Nonlinear Deployment Dynamics and Wrinkling of a Membrane Attached to Two Axially Moving Beams

Behrad Vatankhahghadim* and Christopher J. Damaren†
University of Toronto, Toronto, Ontario M3H 5T6, Canada

https://doi.org/10.2514/1.A34962

The out-of-plane and in-plane deployment dynamics of a flexible space structure, namely, a solar sail quadrant consisting of a membrane attached to two support booms, are considered. The equations of motion of the system are obtained using a time-varying generalization of the extended Hamilton's principle. They are then discretized via quasi-modal expansion of the deflections as truncated series involving both time- and space-dependent basis functions. Because all directions are accounted for and plate strains are used to capture the potentially significant effect of even a small stiffness on the dynamics, nonlinear terms appear in the discretized equations. To increase computational efficiency, coordinate transformations and linear algebraic manipulations are performed to make all spatial integrals time invariant. In addition, attempts are made to predict wrinkling using the Miller–Hedgepeth model: a coarse mesh is defined, the instantaneous state of each region is determined using a wrinkling criterion and averaged principal stresses, and constitutive relation of each region is adjusted based on its wrinkling state. Numerical simulations provide basic validation, sample deployment results, and a comparison against the results of an earlier linear model with only out-of-plane deflections. The stress predictions are also partially validated using previous results based on constant-size loaded membrane experiments.

Nomenclature

A	=	boom cross-sectional area, m^2
B	=	boundary surface of control volume, m^2
$\boldsymbol{C}$	=	constitutive relation matrix
c	=	near-hub distance with uniform density, m
D	=	damping proportionality constant
d	=	base length of wrinkling mesh elements, m
E	=	Young's modulus, N/m^2
$\boldsymbol{e}$	=	boom in-plane generalized coordinates
$\boldsymbol{f}$	=	membrane in-plane generalized coordinates for u
$\boldsymbol{g}$	=	membrane in-plane generalized coordinates for v
g	=	acceleration due to gravity, m/s^2
I	=	second moment of area, m^4
$\hat{\boldsymbol{i}}$	=	unit vector along x axis
$\hat{\boldsymbol{j}}$	=	unit vector along y axis
K	=	number of wrinkling mesh elements on each boom
$\hat{\boldsymbol{k}}$	=	unit vector along z axis
L	=	boom length, m
$\mathcal{L}$	=	Lagrangian, J
n	=	number of discretized quasi modes
$\hat{\boldsymbol{n}}$	=	outward unit normal to boundary of control volume
P	=	axial boom load, N
$\boldsymbol{p}$	=	boom out-of-plane generalized coordinates
$\boldsymbol{q}$	=	membrane out-of-plane generalized coordinates
$\boldsymbol{r}$	=	mass element position vector, m
s	=	membrane thickness, m
$\mathcal{T}$	=	kinetic energy, J
t	=	time, s
$\mathcal{U}$	=	potential energy, J
$\boldsymbol{U}$	=	boundary velocity vector, m/s
u	=	in-plane deflection along x axis, m
$\boldsymbol{V}$	=	deployment velocity vector, m/s
v	=	in-plane deflection along y axis, m
w	=	out-of-plane deflection along z axis, m
$\boldsymbol{x}$	=	states: all generalized coordinates
α	=	outlet distance from origin, m
ϵ	=	strain
ϵ_i	=	ith principal strain
μ	=	membrane density per area, kg/m^2
$\boldsymbol{\nu}$	=	mass element total velocity vector, m/s
ν	=	Poisson's ratio
$\boldsymbol{\xi}$	=	membrane in-plane basis functions
ρ	=	boom density per length, kg/m
σ	=	stress, Pa
$\boldsymbol{\sigma}_i$	=	stress tensor, Pa
σ_i	=	ith principal stress, Pa
$\boldsymbol{\phi}$	=	membrane out-of-plane basis functions
$\boldsymbol{\psi}$	=	boom basis functions

Subscripts

a	=	related to boom (a)
ab	=	related to membrane (ab)
B	=	related to boom
b	=	related to boom (b)
c	=	related to distance c, closed
f	=	final value
M	=	related to membrane
nln	=	nonlinear
o	=	open
S	=	slack
T	=	related to kinetic energy, $\mathcal{T}$; taut
$,t$	=	temporal derivative with respect to t
U	=	related to potential energy, $\mathcal{U}$
uni	=	uniform
W	=	wrinkled
$,x$	=	spatial derivative with respect to x
xx	=	normal component along x
xy	=	shear component along y normal to x
$,y$	=	spatial derivative with respect to y
yx	=	shear component along x normal to y
yy	=	normal component along y
0	=	initial value

Received 18 September 2020; revision received 22 February 2021; accepted for publication 6 March 2021; published online 15 June 2021.

*Doctoral Graduate; currently Research Associate, Institute for Aerospace Studies, 4925 Dufferin Street.

†Professor and Director, Institute for Aerospace Studies, 4925 Dufferin Street. Associate Fellow AIAA.

Superscripts

u	=	related to deflection u
v	=	related to deflection v
w	=	related to deflection w
$\sim$	=	augmented (quadrant-level) variable
$\hat{}$	=	normalized variable or density

Operators

$\delta(\cdot)$	=	variation
$\nabla \cdot (\cdot)$	=	divergence of a vector field

I. Introduction

THIS paper focuses on the deployment dynamics and wrinkling of solar sails, which are among a class of problems involving translating continua. Surveys of studies on different types of such problems, which, in addition to space engineering, also find other applications, such as in the paper industry, elevators, and magnetic tapes, are provided in [1–3]. Given that the problem of this study involves the coupled dynamics of beams and membranes, the reader may also be interested in examples of studies on axially translating beams in [4–7] and axially translating membranes in [8–10]. Of particular relevance to this paper are the past works that used the so-called quasi-modal approach, in which both time- and space-varying basis functions, viewed as snapshots of the modes of the structures at specific times, are used to expand the deflections. Examples of such works in the context of spacecraft applications are [4,11–16]. Focusing specifically on solar sails, there have been a few flown and future missions following the Interplanetary Kitecraft Accelerated by Radiation Of the Sun (the first successful solar sail mission of the world [17]), the most recent and relevant of which (in terms of their boom-supported configurations) include LightSatil 2 [18,19], and the Advanced Composite Solar Sail System [20], which is under development.

Building upon the authors' earlier works in [16,21], this paper also adopts the quasi-modal approach used in the literature for deployment problems because of its simplicity and efficiency compared to the finite element method (FEM) [15]. Whereas [16] focused on the out-of-plane deflections of a single quadrant and [21] extended the formulation to a complete four-quadrant sail upon validating the constant-size modal analysis results against those in [22], this paper introduces the in-plane deflections as well. Using plate strains, this modification results in nonlinear equations of motion (EOM), allows for wrinkling predictions, and eliminates the need for assuming any boundary stress distributions. Some of the simulation results in this paper compare the predictions of the new nonlinear model against those of the linear model in [16] that treated only the out-of-plane deflections, suggesting close predictions but with nonnegligible differences. Despite its much more complicated formulation, the nonlinear model should be considered in lieu of the linear one if more accurate deflection or stress results, or wrinkling predictions are desired. Surveys of studies on nonlinear dynamics of membranes (not necessarily deploying) were provided in [23,24]. For examples of other works on translating continua that introduce geometric and/or material nonlinearity, the reader is referred to [9,25–28].

Unlike the transverse vibration of membranes or plates, to which many works of literature have been dedicated, in-plane vibration of such structures is examined less frequently, perhaps because of the significantly smaller size of such deflections compared to the out-of-plane ones in practical applications. Examples of in-plane vibration studies of plates are [29–31]. More relevant to the deployment problem of interest are [10,32,33], a series of works that treated the in- and/or out-of-plane vibrations of membranes moving on supports separated by fixed distances, motivated by the paper production industry. The inclusion of the in-plane deflections, as is done in the nonlinear model of the present work, also requires a generalization of Hamilton's principle for systems of changing mass, which was accomplished by McIver [34].

The present work also takes interest in wrinkling of a solar sail. A comprehensive examination and comparison of various wrinkle/slack models for use with the FEM studies on membranes were provided in [35], in addition to a new model. It was shown that the following models provide different physical interpretations of an equivalent model: the model in [36], based on the concept of "virtual elongation" such that the recalculated strain matches the real deformations of the wrinkled membrane; that in [37], based on "saturation in elasticity," analogous to the concept of saturation in elastoplastic problems; the model in [38], modifying the strain components in a way that eliminates the stress components that vanish during wrinkling; and that in [39], using the "iterative membrane properties" (IMP) method to modify the constitutive relation, in turn based on the continuum theory of [40]. Also proposed in [35] was a new wrinkle/slack model, the "virtual deformation model" that, in addition to the virtual elongation considered in [36], also incorporates "virtual shear," and hence providing an explicit expression for the wrinkle direction. In addition, building upon the "multiparticle model" for solar sails, Miyazaki and Iwai [41] proposed theoretical considerations for determining the spring constant. With this approach, applied to a spinning solar sail in [41], the spring constant is set to zero for wrinkled regions. In [42], the nonlinear buckling FEM was used to conduct wrinkle analysis, specifically by obtaining the first-order buckling mode. Similarly, application of nonlinear dynamics to the FEM, along with modeling the sail wrinkling using the Miller–Hedgepeth IMP model in [39], was discussed in [43]. The model used in this work is also the Miller–Hedgepeth model, as it lends itself well to the formulation of this project.

The next section describes the model and its simplifying assumptions. Then, the nonlinear dynamics, including all the relevant terms, discretized EOM, and algebraic transformations, and wrinkling studies are treated in separate sections. Lastly, some simulation results are provided, followed by some concluding remarks in the last section.

II. Model Description

This section describes the assumed model and its features. For simplicity of exposition, only one sail quadrant, which consists of a right triangular membrane, attached continuously at all points along its edges to two booms, is considered in this paper. Such a continuous attachment configuration was also considered in [44,45] for distributing the loads more evenly, and resembles Sunjammer (Solar Sail Demonstrator) that was designed to have many periodic attachment points along its booms [46]. First, the simplifying assumptions made to render the problem analytically tractable while capturing its essential features are presented. Then, the spatial distributions of the in-plane velocity, mass density, and stress components consistent with the assumptions are discussed, and lastly, the wrinkling model to be used is presented.

A. Simplifying Assumptions

The sail quadrant is modeled as a thin membrane with a spatially varying areal density and uniform thickness. Unlike [16], in which only the out-of-plane deflections, $w(x, y, t)$, were considered, this paper treats a more complete model that accounts for the in-plane deflections, $u(x, y, t)$ and $v(x, y, t)$, as well. The support booms are modeled as axially rigid (with no deflections along their longitude) cantilevered Euler–Bernoulli beams with uniform density, cross-sectional area, and bending stiffness. They are assumed to have identical physical and geometric properties, and the same constant-rate extension or retraction profiles. A sail quadrant with booms (a) and (b) and membrane (ab) is shown in Fig. 1a, along with their associated deflections. Although relatively small deformations are assumed, nonlinear stress relations are used to capture some of the nonlinearity. Consistent with [16] and as illustrated in Fig. 1b, a sliding-type deployment is assumed, with the free edge of the membrane remaining straight throughout the process. This assumption is reasonable as long as the deployment rate is kept constant. In addition, the membrane is assumed to be under pretension provided by the support booms.

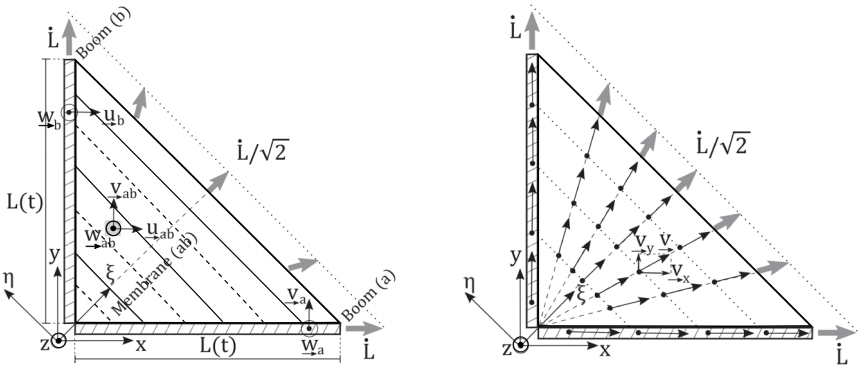

a) Deploying sail quadrant **b) Velocity field**

Fig. 1 Assumed deploying sail quadrant model and its velocity field.

B. Velocity Field

The same velocity field as in [16] and shown in Fig. 1b is used. This field is independent of the in-plane deflection rates (to be added later) and is imposed by the deployment rate of the booms. Consistent with the constant-rate sliding and straight free-edge assumption mentioned earlier, starting from the tilted (ξ, η, z) coordinate system in Fig. 1b and using a 45 deg rotation, we have [16]

$$V_x = \frac{\dot{L}}{2}\left(1 + \frac{x-y}{x+y}\right), \quad V_y = \frac{\dot{L}}{2}\left(1 - \frac{x-y}{x+y}\right) \tag{1}$$

where $V_x(x, y)$ and $V_y(x, y)$ are the x and y components of the deployment velocity of the mass elements. To avoid the singularity at the origin, (0, 0), this mass element is removed from the model and the spatial integrals are taken from small nonzero lower bounds instead (denoted by 0^+). For a spin-deployed sail, accounting for the rotational speed would also be necessary, but assuming the deployment is achieved by linearly extending the booms and given the primary interest in the transient dynamics over the short deployment phase, only the constrained translational dynamics of the deploying sail are considered (disregarding the motion of the hub). For studies on the influence of the deployment rate $\dot{L}$ on the linear stability of a deploying sail (or a quadrant), the reader is referred to [16,21], which adopt energy- and eigenvalue-based approaches to stability analysis, respectively.

C. Density Field

Although uniform membrane areal density was assumed in [16], this would be inconsistent with the ever-increasing length of the free edge and each cross section parallel to it, especially when significant changes in size are expected. This issue is better understood by considering how the mass elements in Fig. 1b are assumed to move further away from each other. To clarify, the material density (in kg/m^3) will remain constant throughout, but because the same amount of material will be distributed over larger areas as the sail deploys, a spatial decrease in the areal density μ (in kg/m^2) is to be expected. The following density field is proposed to provide more consistency between the assumptions:

$$\mu(x, y, t) = \begin{cases} \mu_c \dfrac{L_0}{L(t)}, & \hat{x}(t) + \hat{y}(t) \le \hat{c}_0 \\ \mu_c \dfrac{\hat{c}(t)}{\hat{\xi}(t)} = \mu_c \dfrac{\hat{c}(t)}{\hat{x}(t) + \hat{y}(t)}, & \hat{x}(t) + \hat{y}(t) > \hat{c}_0 \end{cases} \tag{2}$$

where $L_0 = L(0)$ is the initial length of the booms; $\hat{\xi}(t) \triangleq \xi/[L(t)/\sqrt{2}]$ is the normalized distance along the diagonal, corresponding to the tilted (ξ, η, z) coordinate system in Fig. 1a; and $\hat{c}(t) \triangleq c/[L(t)/\sqrt{2}]$ is a small normalized distance on this axis within which a near-origin uniform density is assumed, with $\hat{c}_0 = c/[L_0/\sqrt{2}]$. In addition, $\hat{x}(t) \triangleq x/L(t)$ and $\hat{y}(t) \triangleq y/L(t)$. The density function in Eq. (2) takes a spatially constant value of μ_c for a small distance away from the hub to avoid singularity. There is a temporal decrease in this small region to account for a reduction in the near-hub foldings and to allow for continuity at the $\hat{x} + \hat{y} = \hat{c}_0$ interface. The density then starts dropping proportionally to distance (along the diagonal) beyond that interface, in accordance with the velocity field in Eq. (1) and Fig. 1b. For example, for a small sail that will ultimately have booms of length $L = 10$ m, setting $\mu_c = 50\mu_{\text{uni}}$ with $\hat{c}_0 = 0.01$ ensures the fully deployed sail will have a total mass approximately equal to that with a uniform density of μ_{uni}. Lastly, note that this density field is only reasonable for the constant-rate (nonzero) deployment assumed in this paper, and additional terms may be required if acceleration is involved.

The density field in Eq. (2) can be verified via a mass flow study to ensure conservation of mass m is satisfied: the mass flow rate from a uniform stream of particles through the cross section at $\hat{\xi}(t) = \hat{c}(t)$ is given, in the tilted (ξ, η, z) system, by

$$\dot{m} = \int_{-c}^{c} \mu(\xi, \eta) \cdot V_{\xi}(\xi, \eta)\, \mathrm{d}\eta = \int_{-c}^{c} \mu_c \dot{L}\, \mathrm{d}\eta = 2\mu_c c \dot{L} \tag{3}$$

Applying the 2-D version of the Leibniz integration rule and neglecting the small time-varying portion in the first line of Eq. (2), introduced for numerical considerations only, imply the following relationship in the (x, y, z) coordinate system:

$$\begin{aligned} \dot{m} &= \frac{\mathrm{d}}{\mathrm{d}t} \int_{0^+}^{L(t)} \int_{0^+}^{L(t)-x} \mu(x, y, t)\, \mathrm{d}y\, \mathrm{d}x \\ &= \dot{L} \int_{0^+}^{L(t)} \left[\mu(x, y)\right]_{y=L(t)-x} \mathrm{d}x + \int_{0^+}^{L(t)} \int_{0^+}^{L(t)-x} \underbrace{\frac{\partial}{\partial t}\mu(x, y)}_{\approx 0}\, \mathrm{d}y\, \mathrm{d}x \end{aligned} \tag{4}$$

which, upon conversion to the tilted (ξ, η, z) coordinate system, becomes

$$\begin{aligned} \dot{m} &= \dot{L} \int_{-L(t)/\sqrt{2}}^{L(t)/\sqrt{2}} [\mu(\xi, \eta)]_{\xi = L(t)/\sqrt{2}}\, \mathrm{d}\eta = \dot{L} \int_{-L(t)/\sqrt{2}}^{L(t)/\sqrt{2}} \mu_c \frac{c}{L(t)/\sqrt{2}}\, \mathrm{d}\eta \\ &= 2\mu_c c \dot{L} \end{aligned} \tag{5}$$

Comparing the results in Eqs. (3) and (5) shows that conservation of mass is satisfied, for the mass flow out of the hub matches the actual rate of change of the mass external to it.

D. Stress Field

The formulation of Vatankhahghadim and Damaren [16] based on the Airy function may be problematic for the non-steady-state case of a deployment problem and for cases where the boundary conditions (BCs) are unknown. To alleviate this problem, the nonlinear model that also accounts for the in-plane deflections uses the deflections to determine the strains, which are then used with a suitable constitutive relation to estimate the stresses. The resulting

EOM will be nonlinear, for example, with stiffness matrices that depend on the states.

It was pointed out in [35,47] that even a very small stiffness can play a significant role in the deployment and wrinkling of membranes. As in [28,43], the nonlinear strain terms ϵ are taken to be based on the von Kármán plate theory that incorporates coupling between the out-of-plane deflections w and the in-plane ones u along the x axis and v along the y axis [48]:

$$\epsilon_{xx} = u_{,x} + \frac{1}{2}w_{,x}^2 - zw_{,xx} \tag{6a}$$

$$\epsilon_{yy} = v_{,y} + \frac{1}{2}w_{,y}^2 - zw_{,yy} \tag{6b}$$

$$\epsilon_{xy} = \frac{1}{2}\left(u_{,y} + v_{,x} + w_{,x}w_{,y} - 2zw_{,xy}\right) \tag{6c}$$

where z is the out-of-plane coordinate, with $z = 0$ on the central (neutral) plane. Although some of the previous works, such as [33], used linearized approximations of the strains to compute the stresses, this project maintains the nonlinear forms in both stresses and strains.

E. Wrinkling Model

A coarse mesh is defined, shown in Fig. 2 and only for the purposes of wrinkling state determination, and the constitutive relation is set locally for each mesh element, based on a wrinkling criterion. For example, if a stress-based criterion is used, a region is treated as wrinkled if the minor principal stress is negative, but the major one is positive. This approach should not be confused with the FEM because the global expansions in Eq. (15) are still applicable and the mesh is not used for spatially discretizing the sail to treat its dynamics in a local manner. In this project, the mixed stress/strain criterion from [39,49] is used to select the constitutive relation, because it is deemed to be more robust than the other criteria [43]:

$$\boldsymbol{\sigma} = \boldsymbol{C}\epsilon, \quad \boldsymbol{C} = \begin{cases} \boldsymbol{C}_S, & \epsilon_1 \le 0 \text{ (slack)} \\ \boldsymbol{C}_W, & \epsilon_1 > 0 \text{ and } \nu\epsilon_1 + \epsilon_2 < 0 \text{ (wrinkled)} \\ \boldsymbol{C}_T, & \text{otherwise (taut)} \end{cases} \tag{7}$$

where $\boldsymbol{\sigma} \triangleq [\sigma_{xx}\ \sigma_{yy}\ \sigma_{xy}]^\intercal$ and $\epsilon \triangleq [\epsilon_{xx}\ \epsilon_{yy}\ \epsilon_{xy}]^\intercal$ are stresses and strains, respectively; ϵ_i are principal strains; and $\boldsymbol{C}$ is a suitable constitutive relation [39]:

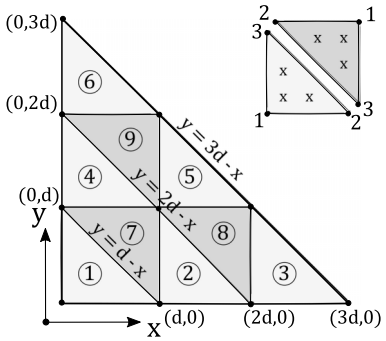

Fig. 2 Mesh for wrinkling studies; top-right: numbers label the corners and crosses (×) show the points used for averaged strains.

$$\boldsymbol{C}_S = \boldsymbol{0}, \qquad \boldsymbol{C}_T = \frac{E}{1-\nu^2}\begin{bmatrix} 1 & \nu & 0 \\ \nu & 1 & 0 \\ 0 & 0 & 1-\nu \end{bmatrix},$$
$$\boldsymbol{C}_W = \frac{E}{4}\begin{bmatrix} 2(1+R) & 0 & 2Q \\ 0 & 2(1-R) & 2Q \\ Q & Q & 2 \end{bmatrix} \tag{8}$$

where $R \triangleq (\epsilon_{xx} - \epsilon_{yy})/(\epsilon_1 - \epsilon_2)$ and $Q \triangleq 2\epsilon_{xy}/(\epsilon_1 - \epsilon_2)$. Also, E and ν are the Young's modulus and Poisson's ratio of the membrane, respectively. The principal strains, ϵ_1 and ϵ_2, are computed as

$$\epsilon_{1,2} = \frac{\epsilon_{xx} + \epsilon_{yy}}{2} \pm \sqrt{\left(\frac{\epsilon_{xx} - \epsilon_{yy}}{2}\right)^2 + \epsilon_{xy}^2} \tag{9}$$

where averaged values are used to obtain single values of ϵ_{xx}, ϵ_{yy}, and ϵ_{xy} for each element. For instance, the stress components at several representative points around the center of each mesh element in Fig. 2 (shown with crosses in the top-right corner of the figure) can be evaluated using Eq. (6) and subsequently combined to yield an average for use in Eqs. (9) and (8).

On the other hand, for analysis purposes and for generating stress contours throughout the membrane, the constitutive relation in Eq. (7) is used with the actual point strains (not the averaged values) obtained by Eq. (6). To this end, the principal stresses, σ_1 and σ_2, at each point are evaluated as

$$\sigma_{1,2} = \frac{\sigma_{xx} + \sigma_{yy}}{2} \pm \sqrt{\left(\frac{\sigma_{xx} - \sigma_{yy}}{2}\right)^2 + \sigma_{xy}^2} \tag{10}$$

where the elasticity matrix corresponding to each mesh element based on Eq. (8) is used along with the constitutive relation in Eq. (7) to obtain the σ_{xx}, σ_{yy}, and σ_{xy} components of each point. Lastly, given that the axial load within the booms must balance out the boundary forces applied by the membrane, we have the following axial loads:

$$P_a = \sigma_{xy}(x, 0, 0)A, \quad P_b = \sigma_{yx}(0, y, 0)A \tag{11}$$

for which known space-dependent functions similar to those in [16] are no longer available. As an average, the midplane ($z = 0$) shear stress of the membrane is assumed throughout the cross sections of the booms.

III. Nonlinear Dynamics

This section treats the nonlinear dynamics of the assumed model by accounting for both in- and out-of-plane deflections. Similar to the approach used for the linear EOM in [16,21], the approach in this paper is based on Lagrangian mechanics, starting from application of a time-varying generalization of the extended Hamilton's principle, due to [34]. Then, the Lagrangian and EOM of a sail quadrant are examined, and to reduce the computational effort, a set of linear algebraic manipulations are subsequently performed on the nonlinear terms. Lastly, the approach for wrinkling predictions is discussed.

A. Use of Hamilton's Principle for Time-Varying Systems

In an Eulerian reference frame (fixed to the hub), the system of interest (external portions of the deploying sail) involves changing mass, and so the extended Hamilton's principle in its classical form is no longer applicable. The following time-varying generalization, however, is available [34]:

$$\delta\int_{t_0}^{t_f}(\mathcal{T}-\mathcal{U})_o\,\mathrm{d}t+\int_{t_0}^{t_f}\left[\iint_{B_c+B_o}\delta r\cdot\boldsymbol{\sigma}\cdot\hat{\boldsymbol{n}}\,\mathrm{d}S+\iint_{B_o}\hat{m}(\boldsymbol{\nu}\cdot\delta\boldsymbol{r})(\boldsymbol{U}-\boldsymbol{\nu})\cdot\hat{\boldsymbol{n}}\mathrm{d}S\right]\mathrm{d}t=0 \tag{12}$$

where $\mathcal{T}$ and $\mathcal{U}$ denote the kinetic and strain energies, respectively; B_o and B_c are the open and closed boundary surfaces, respectively; $\hat{m}$ is the mass density (set to μ or ρ for the membrane or the boom); $\boldsymbol{U}$ is the boundary velocity that is set to zero at the fixed hub outlet; and $\hat{\boldsymbol{n}}$ and $\boldsymbol{\sigma}$ are the unit normal vector and the stress tensor, respectively. Upon permitting the in-plane deflections, their rate of change should also be added, similarly to [33], to the deployment velocity expressions in Eq. (1) to completely describe the velocity $\boldsymbol{\nu}$, of each mass element located at position $\boldsymbol{r}$. Thus

$$\boldsymbol{r}=(x+u)\hat{\boldsymbol{i}}+(y+v)\hat{\boldsymbol{j}}+(z+w)\hat{\boldsymbol{k}} \tag{13a}$$

$$\boldsymbol{\nu}=(V_x+u_{,t}+V_xu_{,x}+V_yu_{,y})\hat{\boldsymbol{i}}+(V_y+v_{,t}+V_xv_{,x}+V_yv_{,y})\hat{\boldsymbol{j}}+(w_{,t}+V_xw_{,x}+V_yw_{,y})\hat{\boldsymbol{k}} \tag{13b}$$

where the deflections along the x, y, and z axes, with unit vectors $\hat{\boldsymbol{i}}$, $\hat{\boldsymbol{j}}$, and $\hat{\boldsymbol{k}}$, are u, v, and w, respectively, and the subscripts after commas denote differentiation. Lastly, V_x and V_y are the deployment velocity components in Eq. (1).

B. Quadrant Lagrangian

Consider the quadrant in Fig. 1a. The kinetic and strain energies, $\mathcal{T}$ and $\mathcal{U}$, of membrane (ab) and boom (a) are influenced by both out-of- and in-plane deflections, and their derivatives

$$\mathcal{T}_{M,ab}=\int_{0^+}^{L(t)}\int_{0^+}^{L(t)-x}\frac{\mu}{2}\boldsymbol{\nu}\cdot\boldsymbol{\nu}\,\mathrm{d}y\,\mathrm{d}x,$$
$$\mathcal{U}_{M,ab}=\int_{-s/2}^{s/2}\int_{0^+}^{L(t)}\int_{0^+}^{L(t)-x}\frac{1}{2}\left[\sigma_{xx}\epsilon_{xx}+\sigma_{yy}\epsilon_{yy}+2\sigma_{xy}\epsilon_{xy}\right]\mathrm{d}y\,\mathrm{d}x\,\mathrm{d}z \tag{14a}$$

$$\mathcal{T}_{B,a}=\int_{0^+}^{L(t)}\frac{\rho}{2}[\boldsymbol{\nu}\cdot\boldsymbol{\nu}]_{y=0}\,\mathrm{d}x,$$
$$\mathcal{U}_{B,a}=\int_{0^+}^{L(t)}\frac{1}{2}\left[EI(w_{a,xx}^2+v_{a,xx}^2)+P_a(w_{a,x}^2+v_{a,x}^2)\right]_{y=0}\mathrm{d}x \tag{14b}$$

where μ and ρ are the membrane and boom mass densities (per area and length, respectively), s is the membrane thickness, EI is the bending stiffness of the booms, and P_a is the axial load on boom (a). Using Eq. (14) and the corresponding boom (b) terms, the Lagrangian for Eq. (12) is obtained as $\mathcal{L}\triangleq(\mathcal{T}_{M,ab}-\mathcal{U}_{M,ab})+(\mathcal{T}_{B,a}-\mathcal{U}_{B,a})+(\mathcal{T}_{B,b}-\mathcal{U}_{B,b})$.

C. Quasi-Modal Expansion

The quasi-modal approach with time-varying basis functions for the out-of-plane deflections used in [16], in turn inspired by [15,50], for example, is extended with the in-plane deflections in mind. The deflections of the booms and those of the membrane (superimposed over the former) are expanded as

$$w_a(x,t)=\boldsymbol{p}_a^{\mathsf{T}}(t)\boldsymbol{\psi}_a(x,t),\quad w_b(y,t)=\boldsymbol{p}_b^{\mathsf{T}}(t)\boldsymbol{\psi}_b(y,t)$$
$$w_{ab}(x,y,t)=w_a(x,t)+w_b(y,t)+\boldsymbol{q}_{ab}^{\mathsf{T}}(t)\boldsymbol{\phi}_{ab}(x,y,t) \tag{15a}$$

$$u_{\mathrm{a}}(x,t)=0\ ,\ \ u_{\mathrm{b}}(y,t)=\boldsymbol{e}_{\mathrm{b}}^{\mathsf{T}}(t)\boldsymbol{\psi}_{\mathrm{b}}(y,t)$$
$$u_{\mathrm{ab}}(x,y,t)=\cancelto{0}{u_{\mathrm{a}}(x,t)}+u_{\mathrm{b}}(y,t)+\boldsymbol{f}_{\mathrm{ab}}^{\mathsf{T}}(t)\boldsymbol{\xi}_{\mathrm{ab}}^{\mathrm{u}}(x,y,t) \tag{15b}$$

$$v_{\mathrm{a}}(x,t)=\boldsymbol{e}_{\mathrm{a}}^{\mathsf{T}}(t)\boldsymbol{\psi}_{\mathrm{a}}(x,t)\ ,\ \ v_{\mathrm{b}}(y,t)=0$$
$$v_{\mathrm{ab}}(x,y,t)=v_{\mathrm{a}}(x,t)+\cancelto{0}{v_{\mathrm{b}}(y,t)}+\boldsymbol{g}_{\mathrm{ab}}^{\mathsf{T}}(t)\boldsymbol{\xi}_{\mathrm{ab}}^{\mathrm{v}}(x,y,t) \tag{15c}$$

from which $\boldsymbol{x}\triangleq[\boldsymbol{p}_a^{\mathsf{T}}\ \boldsymbol{p}_b^{\mathsf{T}}\ \boldsymbol{q}_{ab}^{\mathsf{T}}\ \boldsymbol{e}_b^{\mathsf{T}}\ \boldsymbol{f}_{ab}^{\mathsf{T}}\ \boldsymbol{e}_a^{\mathsf{T}}\ \boldsymbol{g}_{ab}^{\mathsf{T}}]^{\mathsf{T}}$ is defined to contain all generalized coordinates, with each block a column matrix of size n_B or n_M, the number of boom or membrane quasi modes. Note that $u_a=0$ and $v_b=0$ owing to the axial rigidity assumption on the booms. The time-varying components of $\boldsymbol{\psi}$, $\boldsymbol{\phi}$, $\boldsymbol{\xi}^u$, and $\boldsymbol{\xi}^v$, which contain the basis functions for the deflections of the booms, the out-of-plane deflections of the membrane, and the in-plane deflections of the membrane along the x and y axes, respectively, depend on $x/L(t)$ and/or $y/L(t)$. Given that the out-of-plane and in-plane deflections of the membrane have the same BCs along the edges, their basis functions (the components of $\boldsymbol{\phi}$, $\boldsymbol{\xi}^u$, and $\boldsymbol{\xi}^v$) are all set to be the same. The following functions, based on the eigenfunctions of a cantilevered beam and a square membrane with all edges clamped from [51], are used:

$$\psi_k(x,t)=\cos\left(\beta_k\frac{x}{L(t)}\right)-\cosh\left(\beta_k\frac{x}{L(t)}\right)-\kappa_k\left[\sin\left(\beta_k\frac{x}{L(t)}\right)-\sinh\left(\beta_k\frac{x}{L(t)}\right)\right] \tag{16a}$$

$$\phi_k(x,y,t)=\sin\left(i\pi\frac{x}{L(t)}\right)\sin\left(j\pi\frac{y}{L(t)}\right) \tag{16b}$$

$$\xi_k^u(x,y,t)=\sin\left(i\pi\frac{x}{L(t)}\right)\sin\left(j\pi\frac{y}{L(t)}\right)=\xi_k^v(x,y,t) \tag{16c}$$

where $\{i,j\}\in\{1,2,\ldots,\sqrt{n_M}\}$ are ordered pairs of coefficients corresponding to the kth mode out of a total of n_M membrane modes. The variables β_k are the solutions of $\cos(\beta_k)\cosh(\beta_k)+1=0$, and κ_k is defined as $\kappa_k\triangleq[\cos(\beta_k)+\cosh(\beta_k)]/[\sin(\beta_k)+\sinh(\beta_k)]$ [52].

D. Transformed System Matrices: Linear Terms

The coordinate transformation discussed in [16], in which new normalized coordinates between 0 and 1 are defined as $\hat{x}\triangleq x/L(t)$ and $\hat{y}\triangleq y/L(t)$, is adapted, necessitating the use of the following space and time derivatives corresponding to the transformed coordinates:

$$\frac{\partial}{\partial x}(\cdot)=\frac{1}{L}\frac{\partial}{\partial\hat{x}}(\cdot),\qquad\frac{\partial}{\partial y}(\cdot)=\frac{1}{L}\frac{\partial}{\partial\hat{y}}(\cdot) \tag{17a}$$

$$\frac{\partial^2}{\partial x^2}(\cdot)=\frac{1}{L^2}\frac{\partial^2}{\partial\hat{x}^2}(\cdot),\quad\frac{\partial^2}{\partial y^2}(\cdot)=\frac{1}{L^2}\frac{\partial^2}{\partial\hat{y}^2}(\cdot),\quad\frac{\partial^2}{\partial x\partial y}(\cdot)=\frac{1}{L^2}\frac{\partial^2}{\partial\hat{x}\partial\hat{y}}(\cdot) \tag{17b}$$

$$\left.\frac{\partial}{\partial t}(\cdot)\right|_{(x,y)}=\left.\frac{\partial}{\partial t}(\cdot)\right|_{(\hat{x},\hat{y})}-\left.\frac{\hat{x}\dot{L}}{L}\frac{\partial}{\partial\hat{x}}(\cdot)\right|_{(\hat{x},\hat{y})}-\left.\frac{\hat{y}\dot{L}}{L}\frac{\partial}{\partial\hat{y}}(\cdot)\right|_{(\hat{x},\hat{y})} \tag{17c}$$

using which the following boom-related matrices are obtained [excluding the strain energy from the compression of the booms, the second term in the integrand of $\mathcal{U}_{B,a}$ in Eq. (14b), to be treated in the last subsection of this section]:

$$\boldsymbol{M}_B=\rho L(t)\int_{0^+}^{1}\boldsymbol{\psi}_a(\hat{x})\boldsymbol{\psi}_a^{\mathsf{T}}(\hat{x})\,\mathrm{d}\hat{x} \tag{18a}$$

$$\boldsymbol{G}_B=\rho\dot{L}\int_{0^+}^{1}(1-\hat{x})\boldsymbol{\psi}_a(\hat{x})\boldsymbol{\psi}_{a,\hat{x}}^{\mathsf{T}}(\hat{x})\,\mathrm{d}\hat{x} \tag{18b}$$

$$\boldsymbol{K}_{B,T}=\rho\frac{\dot{L}^2}{L(t)}\int_{0^+}^{1}(1-\hat{x})^2\boldsymbol{\psi}_{a,\hat{x}}(\hat{x})\boldsymbol{\psi}_{a,\hat{x}}^{\mathsf{T}}(\hat{x})\,\mathrm{d}\hat{x} \tag{18c}$$

$$\boldsymbol{K}_{B,U,2} = \frac{EI}{L^3(t)} \int_{0^+}^{1} \boldsymbol{\psi}_{a,\hat{x}\hat{x}}(\hat{x}) \boldsymbol{\psi}_{a,\hat{x}\hat{x}}^{\intercal}(\hat{x})\, \mathrm{d}\hat{x} \tag{18d}$$

where $\boldsymbol{\psi}_a(\hat{x})$ stores the beam eigenfunctions in terms of $\hat{x}$, and $\boldsymbol{\psi}_{a,\hat{x}}(\hat{x}) = L(t)\boldsymbol{\psi}_{a,x}(x,t)$ and $\boldsymbol{\psi}_{a,\hat{x}\hat{x}}(\hat{x}) = L^2(t)\boldsymbol{\psi}_{a,xx}(x,t)$ are its spatial derivatives with respect to $\hat{x}$. Because all of the integrals in Eq. (18) are only $\hat{x}$ dependent, numerical integration in the absence of analytical expressions is required only once, and not at each time step. For later use in the nonlinear EOM in Eq. (33), the matrices in Eq. (18) are placed in quadrant-level augmented $n \times n$ block-diagonal form corresponding to $\boldsymbol{x}$, with $\boldsymbol{0}_{n_M \times n_M}$ blocks associated with the membrane generalized coordinates. For example

$$\tilde{\boldsymbol{M}}_B \triangleq \text{blockdiag}\{\boldsymbol{M}_B, \boldsymbol{M}_B, \boldsymbol{0}, \boldsymbol{M}_B, \boldsymbol{0}, \boldsymbol{M}_B, \boldsymbol{0}\} \tag{19}$$

To achieve time independence of the density field in Eq. (2), but allow for its space dependence, we can define $\hat{\mu} = L(t) \cdot \mu$ as follows:

$$\hat{\mu}(\hat{x}, \hat{y}) = \begin{cases} \mu_c L_0, & \hat{x} + \hat{y} \le \hat{c}_0 \\ \mu_c \dfrac{c\sqrt{2}}{\hat{x} + \hat{y}}, & \hat{x} + \hat{y} > \hat{c}_0 \end{cases} \tag{20}$$

Using this density function, the following membrane-related matrices are obtained [excluding the strain energy owing to the stress field, namely, $\mathcal{U}_{M,ab}$ in Eq. (14a), to be treated in the last subsection of this section]:

$$\tilde{\boldsymbol{M}}_M = L(t) \int_{0^+}^{1} \int_{0^+}^{1-\hat{x}} \hat{\mu} \begin{bmatrix} \hat{\boldsymbol{a}}^w \hat{\boldsymbol{a}}^{w\intercal} & \boldsymbol{0} & \boldsymbol{0} \\ \boldsymbol{0} & \hat{\boldsymbol{a}}^u \hat{\boldsymbol{a}}^{u\intercal} & \boldsymbol{0} \\ \boldsymbol{0} & \boldsymbol{0} & \hat{\boldsymbol{a}}^v \hat{\boldsymbol{a}}^{v\intercal} \end{bmatrix} \mathrm{d}\hat{y}\, \mathrm{d}\hat{x} \tag{21a}$$

$$\tilde{\boldsymbol{G}}_M = \dot{L} \int_{0^+}^{1} \int_{0^+}^{1-\hat{x}} \hat{\mu} \begin{bmatrix} \hat{\boldsymbol{a}}^w \hat{\boldsymbol{b}}^{w\intercal} & \boldsymbol{0} & \boldsymbol{0} \\ \boldsymbol{0} & \hat{\boldsymbol{a}}^u \hat{\boldsymbol{b}}^{u\intercal} & \boldsymbol{0} \\ \boldsymbol{0} & \boldsymbol{0} & \hat{\boldsymbol{a}}^v \hat{\boldsymbol{b}}^{v\intercal} \end{bmatrix} \mathrm{d}\hat{y}\, \mathrm{d}\hat{x} \tag{21b}$$

$$\tilde{\boldsymbol{K}}_{M,T} = \frac{\dot{L}^2}{L(t)} \int_{0^+}^{1} \int_{0^+}^{1-\hat{x}} \hat{\mu} \begin{bmatrix} \hat{\boldsymbol{b}}^w \hat{\boldsymbol{b}}^{w\intercal} & \boldsymbol{0} & \boldsymbol{0} \\ \boldsymbol{0} & \hat{\boldsymbol{b}}^u \hat{\boldsymbol{b}}^{u\intercal} & \boldsymbol{0} \\ \boldsymbol{0} & \boldsymbol{0} & \hat{\boldsymbol{b}}^v \hat{\boldsymbol{b}}^{v\intercal} \end{bmatrix} \mathrm{d}\hat{y}\, \mathrm{d}\hat{x} \tag{21c}$$

$$\tilde{\boldsymbol{\alpha}}_M = \dot{L} L(t) \int_{0^+}^{1} \int_{0^+}^{1-\hat{x}} \hat{\mu} \begin{bmatrix} \boldsymbol{0} \\ \hat{V}_x \hat{\boldsymbol{a}}^u \\ \hat{V}_y \hat{\boldsymbol{a}}^v \end{bmatrix} \mathrm{d}\hat{y}\, \mathrm{d}\hat{x} \tag{21d}$$

$$\tilde{\boldsymbol{\beta}}_M = \dot{L}^2 \int_{0^+}^{1} \int_{0^+}^{1-\hat{x}} \hat{\mu} \begin{bmatrix} \boldsymbol{0} \\ \hat{V}_x \hat{\boldsymbol{b}}^u \\ \hat{V}_y \hat{\boldsymbol{b}}^v \end{bmatrix} \mathrm{d}\hat{y}\, \mathrm{d}\hat{x} \tag{21e}$$

for which the following intermediate matrices are defined:

$$\hat{\boldsymbol{a}}^w(\hat{x}, \hat{y}) \triangleq \begin{bmatrix} \boldsymbol{\psi}_a(\hat{x}) \\ \boldsymbol{\psi}_b(\hat{y}) \\ \boldsymbol{\phi}_{ab}(\hat{x}, \hat{y}) \end{bmatrix},$$

$$\hat{\boldsymbol{b}}^w(\hat{x}, \hat{y}) \triangleq \begin{bmatrix} (\hat{V}_x - \hat{x})\boldsymbol{\psi}_{a,\hat{x}}(\hat{x}) \\ (\hat{V}_y - \hat{y})\boldsymbol{\psi}_{b,\hat{y}}(\hat{y}) \\ (\hat{V}_x - \hat{x})\boldsymbol{\phi}_{ab,\hat{x}}(\hat{x}, \hat{y}) + (\hat{V}_y - \hat{y})\boldsymbol{\phi}_{ab,\hat{y}}(\hat{x}, \hat{y}) \end{bmatrix} \tag{22a}$$

$$\hat{\boldsymbol{a}}^u(\hat{x}, \hat{y}) \triangleq \begin{bmatrix} \boldsymbol{\psi}_b(\hat{y}) \\ \boldsymbol{\xi}^u_{ab}(\hat{x}, \hat{y}) \end{bmatrix},$$

$$\hat{\boldsymbol{b}}^u(\hat{x}, \hat{y}) \triangleq \begin{bmatrix} (\hat{V}_y - \hat{y})\boldsymbol{\psi}_{b,\hat{y}}(\hat{y}) \\ (\hat{V}_x - \hat{x})\boldsymbol{\xi}^u_{ab,\hat{x}}(\hat{x}, \hat{y}) + (\hat{V}_y - \hat{y})\boldsymbol{\xi}^u_{ab,\hat{y}}(\hat{x}, \hat{y}) \end{bmatrix} \tag{22b}$$

$$\hat{\boldsymbol{a}}^v(\hat{x}, \hat{y}) \triangleq \begin{bmatrix} \boldsymbol{\psi}_a(\hat{x}) \\ \boldsymbol{\xi}^v_{ab}(\hat{x}, \hat{y}) \end{bmatrix},$$

$$\hat{\boldsymbol{b}}^v(\hat{x}, \hat{y}) \triangleq \begin{bmatrix} (\hat{V}_x - \hat{x})\boldsymbol{\psi}_{a,\hat{x}}(\hat{x}) \\ (\hat{V}_x - \hat{x})\boldsymbol{\xi}^v_{ab,\hat{x}}(\hat{x}, \hat{y}) + (\hat{V}_y - \hat{y})\boldsymbol{\xi}^v_{ab,\hat{y}}(\hat{x}, \hat{y}) \end{bmatrix} \tag{22c}$$

where $\hat{V}_x \triangleq V_x/\dot{L}$ and $\hat{V}_y \triangleq V_y/\dot{L}$ are the rate-normalized analogs of the velocity field components in Eq. (1). These matrices could be extended in a form corresponding to the complete quadrant-level generalized coordinates $\boldsymbol{x}$ as

$$\tilde{\boldsymbol{a}}^w \triangleq \begin{bmatrix} \hat{\boldsymbol{a}}^w \\ \boldsymbol{0} \\ \boldsymbol{0} \end{bmatrix}, \quad \tilde{\boldsymbol{a}}^u \triangleq \begin{bmatrix} \boldsymbol{0} \\ \hat{\boldsymbol{a}}^u \\ \boldsymbol{0} \end{bmatrix}, \quad \tilde{\boldsymbol{a}}^v \triangleq \begin{bmatrix} \boldsymbol{0} \\ \boldsymbol{0} \\ \hat{\boldsymbol{a}}^v \end{bmatrix},$$

$$\tilde{\boldsymbol{b}}^w \triangleq \begin{bmatrix} \hat{\boldsymbol{b}}^w \\ \boldsymbol{0} \\ \boldsymbol{0} \end{bmatrix}, \quad \tilde{\boldsymbol{b}}^u \triangleq \begin{bmatrix} \boldsymbol{0} \\ \hat{\boldsymbol{b}}^u \\ \boldsymbol{0} \end{bmatrix}, \quad \tilde{\boldsymbol{b}}^v \triangleq \begin{bmatrix} \boldsymbol{0} \\ \boldsymbol{0} \\ \hat{\boldsymbol{b}}^v \end{bmatrix} \tag{23}$$

which will simplify the notation in the subsequent sections. The same comments as those made about the computational efficiency of evaluating the time-invariant integrals of Eq. (18) hold with regard to those in Eq. (21).

E. Transformed System Matrices: Nonlinear Terms

Some algebraic operations will be performed in the next subsection on the terms involved in the nonlinear model to increase numerical efficiency. In preparation for these operations, the discretized deflections of the membrane in Eq. (15) are written in terms of the complete states as

$$w_{ab} = \boldsymbol{x}^{\intercal} \tilde{\boldsymbol{a}}^w \tag{24a}$$

$$u_{ab} = \boldsymbol{x}^{\intercal} \tilde{\boldsymbol{a}}^u \tag{24b}$$

$$v_{ab} = \boldsymbol{x}^{\intercal} \tilde{\boldsymbol{a}}^v \tag{24c}$$

where $\tilde{\boldsymbol{a}}^w$, $\tilde{\boldsymbol{a}}^u$, and $\tilde{\boldsymbol{a}}^v$, as defined in Eq. (23), are employed. Then, using Eq. (17), the strain terms in Eq. (6) are rewritten as

$$\epsilon_{xx} = \frac{1}{L}\left[\boldsymbol{x}^{\intercal}\left(\tilde{\boldsymbol{a}}^u_{,\hat{x}} - \frac{z}{L}\tilde{\boldsymbol{a}}^w_{,\hat{x}\hat{x}}\right) + \frac{1}{2L}\boldsymbol{x}^{\intercal}(\tilde{\boldsymbol{a}}^w_{,\hat{x}}\tilde{\boldsymbol{a}}^{w\intercal}_{,\hat{x}})\boldsymbol{x}\right] \tag{25a}$$

$$\epsilon_{yy} = \frac{1}{L}\left[\boldsymbol{x}^{\intercal}\left(\tilde{\boldsymbol{a}}^v_{,\hat{y}} - \frac{z}{L}\tilde{\boldsymbol{a}}^w_{,\hat{y}\hat{y}}\right) + \frac{1}{2L}\boldsymbol{x}^{\intercal}(\tilde{\boldsymbol{a}}^w_{,\hat{y}}\tilde{\boldsymbol{a}}^{w\intercal}_{,\hat{y}})\boldsymbol{x}\right] \tag{25b}$$

$$\epsilon_{xy} = \frac{1}{2L}\left[\boldsymbol{x}^{\intercal}\left(\tilde{\boldsymbol{a}}^u_{,\hat{y}} + \tilde{\boldsymbol{a}}^v_{,\hat{x}} - 2\frac{z}{L}\tilde{\boldsymbol{a}}^w_{,\hat{x}\hat{y}}\right) + \frac{1}{2L}\boldsymbol{x}^{\intercal}(2\tilde{\boldsymbol{a}}^w_{,\hat{x}}\tilde{\boldsymbol{a}}^{w\intercal}_{,\hat{y}})\boldsymbol{x}\right] \tag{25c}$$

The stress components are rewritten in a similar manner. Based on the constitutive relation in Eq. (7) and the regular Hookean elasticity matrix, $\boldsymbol{C}_T$ in Eq. (8), the stresses in the taut region satisfy:

$$\sigma_{T,xx} = \frac{E}{(1-\nu^2)L}\left[\boldsymbol{x}^{\intercal}\left(\tilde{\boldsymbol{a}}^u_{,\hat{x}} + \nu\tilde{\boldsymbol{a}}^v_{,\hat{y}} - \frac{z}{L}\left(\tilde{\boldsymbol{a}}^w_{,\hat{x}\hat{x}} + \nu\tilde{\boldsymbol{a}}^w_{,\hat{y}\hat{y}}\right)\right) + \frac{1}{2L}\boldsymbol{x}^{\intercal}\left(\tilde{\boldsymbol{a}}^w_{,\hat{x}}\tilde{\boldsymbol{a}}^{w\intercal}_{,\hat{x}} + \nu\tilde{\boldsymbol{a}}^w_{,\hat{y}}\tilde{\boldsymbol{a}}^{w\intercal}_{,\hat{y}}\right)\boldsymbol{x}\right] \tag{26a}$$

$$\sigma_{T,yy} = \frac{E}{(1-\nu^2)L}\left[\boldsymbol{x}^{\intercal}\left(\nu\tilde{\boldsymbol{a}}^u_{,\hat{x}} + \tilde{\boldsymbol{a}}^v_{,\hat{y}} - \frac{z}{L}\left(\nu\tilde{\boldsymbol{a}}^w_{,\hat{x}\hat{x}} + \tilde{\boldsymbol{a}}^w_{,\hat{y}\hat{y}}\right)\right) + \frac{1}{2L}\boldsymbol{x}^{\intercal}\left(\nu\tilde{\boldsymbol{a}}^w_{,\hat{x}}\tilde{\boldsymbol{a}}^{w\intercal}_{,\hat{x}} + \tilde{\boldsymbol{a}}^w_{,\hat{y}}\tilde{\boldsymbol{a}}^{w\intercal}_{,\hat{y}}\right)\boldsymbol{x}\right] \tag{26b}$$

$$\sigma_{T,xy} = \frac{E}{2(1+\nu)L}\left[\boldsymbol{x}^{\intercal}\left(\tilde{\boldsymbol{a}}^{u}_{,\hat{y}} + \tilde{\boldsymbol{a}}^{v}_{,\hat{x}} - 2\frac{z}{L}\tilde{\boldsymbol{a}}^{w}_{,\hat{x}\hat{y}}\right) + \frac{1}{2L}\boldsymbol{x}^{\intercal}\left(2\tilde{\boldsymbol{a}}^{w}_{,\hat{x}}\tilde{\boldsymbol{a}}^{w\intercal}_{,\hat{y}}\right)\boldsymbol{x}\right] \tag{26c}$$

In addition, referring back to Eq. (7) but using the adjusted elasticity matrix, $\boldsymbol{C}_W$ in Eq. (8), the stress components in the wrinkled region satisfy:

$$\sigma_{W,xx} = \frac{E}{4L}\left[\boldsymbol{x}^{\intercal}\left(2(1+R)\tilde{\boldsymbol{a}}^{u}_{,\hat{x}} + Q\left(\tilde{\boldsymbol{a}}^{u}_{,\hat{y}} + \tilde{\boldsymbol{a}}^{v}_{,\hat{x}}\right) - \frac{z}{L}\left(2(1+R)\tilde{\boldsymbol{a}}^{w}_{,\hat{x}\hat{x}} + 2Q\tilde{\boldsymbol{a}}^{w}_{,\hat{x}\hat{y}}\right)\right) + \frac{1}{2L}\boldsymbol{x}^{\intercal}\left(2(1+R)\tilde{\boldsymbol{a}}^{w}_{,\hat{x}}\tilde{\boldsymbol{a}}^{w\intercal}_{,\hat{x}} + 2Q\tilde{\boldsymbol{a}}^{w}_{,\hat{x}}\tilde{\boldsymbol{a}}^{w\intercal}_{,\hat{y}}\right)\boldsymbol{x}\right] \tag{27a}$$

$$\sigma_{W,yy} = \frac{E}{4L}\left[\boldsymbol{x}^{\intercal}\left(2(1-R)\tilde{\boldsymbol{a}}^{v}_{,\hat{y}} + Q\left(\tilde{\boldsymbol{a}}^{u}_{,\hat{y}} + \tilde{\boldsymbol{a}}^{v}_{,\hat{x}}\right) - \frac{z}{L}\left(2(1-R)\tilde{\boldsymbol{a}}^{w}_{,\hat{y}\hat{y}} + 2Q\tilde{\boldsymbol{a}}^{w}_{,\hat{x}\hat{y}}\right)\right) + \frac{1}{2L}\boldsymbol{x}^{\intercal}\left(2(1-R)\tilde{\boldsymbol{a}}^{w}_{,\hat{y}}\tilde{\boldsymbol{a}}^{w\intercal}_{,\hat{y}} + 2Q\tilde{\boldsymbol{a}}^{w}_{,\hat{x}}\tilde{\boldsymbol{a}}^{w\intercal}_{,\hat{y}}\right)\boldsymbol{x}\right] \tag{27b}$$

$$\sigma_{W,xy} = \frac{E}{4L}\left[\boldsymbol{x}^{\intercal}\left(Q\left(\tilde{\boldsymbol{a}}^{u}_{,\hat{x}} + \tilde{\boldsymbol{a}}^{v}_{,\hat{y}}\right) + \left(\tilde{\boldsymbol{a}}^{u}_{,\hat{y}} + \tilde{\boldsymbol{a}}^{v}_{,\hat{x}}\right) - \frac{z}{L}\left(Q\tilde{\boldsymbol{a}}^{w}_{,\hat{x}\hat{x}} + Q\tilde{\boldsymbol{a}}^{w}_{,\hat{y}\hat{y}} + 2\tilde{\boldsymbol{a}}^{w}_{,\hat{x}\hat{y}}\right)\right) + \frac{1}{2L}\boldsymbol{x}^{\intercal}\left(Q\tilde{\boldsymbol{a}}^{w}_{,\hat{x}}\tilde{\boldsymbol{a}}^{w\intercal}_{,\hat{x}} + Q\tilde{\boldsymbol{a}}^{w}_{,\hat{y}}\tilde{\boldsymbol{a}}^{w\intercal}_{,\hat{y}} + 2\tilde{\boldsymbol{a}}^{w}_{,\hat{x}}\tilde{\boldsymbol{a}}^{w\intercal}_{,\hat{y}}\right)\boldsymbol{x}\right] \tag{27c}$$

The boom compression terms in Eq. (14b) are then set to $P_a = A\sigma_{xy}(x,0,0)$ and $P_b = A\sigma_{xy}(0,y,0)$ from Eq. (11), where, as an average, the midplane ($z = 0$) shear stress of the membrane is assumed throughout the cross-sectional area A of the booms.

1. Contribution from Strain Energy

As mentioned earlier, the matrices in Eqs. (18) and (21) do not capture parts of the boom and membrane strain energies in Eqs. (14b) and (14a). The following nonlinear (in states) terms are to appear in the EOM in Eq. (33) as contribution of these remaining portions to the Lagrangian in Eq. (12):

$$\tilde{\boldsymbol{k}}_{M,\mathrm{nln}} = \frac{\partial \mathcal{U}_{M,ab}}{\partial \boldsymbol{x}} = L^2\frac{\partial}{\partial \boldsymbol{x}}\int_{-s/2}^{s/2}\int_{0^+}^{1}\int_{0^+}^{1-\hat{x}}\frac{1}{2}[\sigma_{xx}\epsilon_{xx} + \sigma_{yy}\epsilon_{yy} + 2\sigma_{xy}\epsilon_{xy}]\,\mathrm{d}\hat{y}\,\mathrm{d}\hat{x}\,\mathrm{d}z \tag{28a}$$

$$\tilde{\boldsymbol{k}}_{B,\mathrm{nln}} = L\frac{\partial}{\partial \boldsymbol{x}}\int_{0^+}^{1}\frac{1}{2}\left[P_a(w_{a,x}^2 + v_{a,x}^2)\right]_{y=0}\mathrm{d}\hat{x} + L\frac{\partial}{\partial \boldsymbol{x}}\int_{0^+}^{1}\frac{1}{2}\left[P_b(w_{b,y}^2 + u_{b,y}^2)\right]_{x=0}\mathrm{d}\hat{y} \tag{28b}$$

In a numerical framework, the preceding differentiations with respect to states can be handled symbolically. However, owing to the complicated expressions and the time-varying nature of the spatial triple integrals in their present form, to be reevaluated at each time step, the symbolic approach was determined to be prohibitively computationally expensive. To alleviate this issue, some algebraic operations, presented in Subsection G, can be performed to eliminate the state dependence of the spatial integrals.

2. Contribution from Outlet Work and Momentum Transfer

An assumption is needed about the outlet of the hub through which mass flow occurs. Two possibilities are shown in Fig. 3. The circular shape in Fig. 3a would be mathematically convenient because the unit normal and velocity vectors along it would be parallel, but such an interface may introduce practical or production difficulties in a real system. Assuming the linear shape in Fig. 3b, parallel to the free edge and from $x = \alpha$ on Boom (a) to $y = \alpha$ on boom (b), the work and momentum transport terms in Eq. (12) are

$$\begin{aligned}\iint_{B_c+B_o}\delta\boldsymbol{r}\cdot\boldsymbol{\sigma}\cdot\hat{\boldsymbol{n}}\,\mathrm{d}S &= \int_{-s/2}^{s/2}\int_{0^+}^{\alpha}\begin{bmatrix}\delta u\\ \delta v\end{bmatrix}^{\intercal}\begin{bmatrix}\sigma_{xx} & \sigma_{xy}\\ \sigma_{xy} & \sigma_{yy}\end{bmatrix}\left(\frac{-\sqrt{2}}{2}\begin{bmatrix}1\\1\end{bmatrix}\right)\Bigg|_{y=\alpha-x}\mathrm{d}x\,\mathrm{d}y\\ &= -\frac{\sqrt{2}}{2}L\int_{-s/2}^{s/2}\int_{0^+}^{\alpha/L}[(\sigma_{xx}+\sigma_{xy})\delta u + (\sigma_{yy}+\sigma_{xy})\delta v]_{\hat{y}=(\alpha/L)-\hat{x}}\,\mathrm{d}\hat{x}\,\mathrm{d}z\end{aligned} \tag{29a}$$

$$\begin{aligned}\iint_{\mathrm{B_o}}\hat{m}\,(\boldsymbol{\nu}\cdot\delta\boldsymbol{r})\left(\cancelto{\boldsymbol{0}}{\boldsymbol{V}} - \boldsymbol{\nu}\right)\cdot\hat{\boldsymbol{n}}\,\mathrm{d}S &= \int_{-s/2}^{s/2}\int_{0^+}^{\alpha}\mu\begin{bmatrix}\nu_{\mathrm{x}}\\ \nu_{\mathrm{y}}\end{bmatrix}^{\intercal}\begin{bmatrix}\delta u\\ \delta v\end{bmatrix}\left(\frac{\sqrt{2}}{2}\begin{bmatrix}1\\1\end{bmatrix}\right)^{\intercal}\begin{bmatrix}\nu_{\mathrm{x}}\\ \nu_{\mathrm{y}}\end{bmatrix}\Bigg|_{y=\alpha-x}\mathrm{d}x\,\mathrm{d}z\\ &= \frac{\sqrt{2}}{2}s\int_{0^+}^{\alpha/L}\left[\hat{\mu}(\nu_{\mathrm{x}}+\nu_{\mathrm{y}})(\nu_{\mathrm{x}}\delta u + \nu_{\mathrm{y}}\delta v)\right]_{\hat{y}=(\alpha/L)-\hat{x}}\mathrm{d}\hat{x}\end{aligned} \tag{29b}$$

where the vertical deflection along the outlet is constrained by $\delta w \equiv 0$, resulting in no contribution from the booms (because they are also assumed to be axially rigid) and the following variation of the position vector in Eq. (13a):

$$\begin{aligned}\delta\boldsymbol{r} = \delta(x+u)\hat{\boldsymbol{i}} + \delta(y+v)\hat{\boldsymbol{j}} + \delta(z+w)\hat{\boldsymbol{k}} &= \delta u\hat{\boldsymbol{i}} + \delta v\hat{\boldsymbol{j}} + \cancelto{0}{\delta w\hat{\boldsymbol{k}}}\\ &= \left(\tilde{\boldsymbol{a}}^{\mathrm{u}\intercal}\delta\boldsymbol{x}\right)\hat{\boldsymbol{i}} + \left(\tilde{\boldsymbol{a}}^{\mathrm{v}\intercal}\delta\boldsymbol{x}\right)\hat{\boldsymbol{j}}\end{aligned} \tag{30}$$

where the modal expansion of Eq. (24) is used. In addition, the x and y components of the velocity of the mass elements in Eq. (13b), expressed in terms of $\hat{x}$ and $\hat{y}$, are given by

$$\nu_x = \dot{L}\hat{V}_x + \dot{\boldsymbol{x}}^{\intercal}\tilde{\boldsymbol{a}}^{u} + \frac{\dot{L}}{L}\boldsymbol{x}^{\intercal}\tilde{\boldsymbol{b}}^{u} \tag{31a}$$

$$\nu_y = \dot{L}\hat{V}_y + \dot{\boldsymbol{x}}^{\intercal}\tilde{\boldsymbol{a}}^{v} + \frac{\dot{L}}{L}\boldsymbol{x}^{\intercal}\tilde{\boldsymbol{b}}^{v} \tag{31b}$$

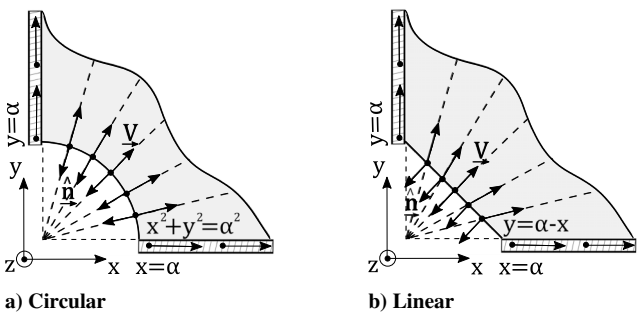

a) Circular **b) Linear**

Fig. 3 Two possible hub outlet shapes.

where $\tilde{\boldsymbol{a}}^u$, $\tilde{\boldsymbol{a}}^v$, $\tilde{\boldsymbol{b}}^u$, and $\tilde{\boldsymbol{b}}^v$ are as defined in Eq. (23). After substituting the expressions in Eqs. (29–31) into the generalization of Hamilton's principle in Eq. (12) and factoring $\delta\boldsymbol{x}$ out of the spatial integrals, the following column matrices appear in the EOM:

$$\tilde{\boldsymbol{w}}_M = -\frac{\sqrt{2}}{2}L \times \int_{-s/2}^{s/2}\int_{0^+}^{\alpha/L}[(\sigma_{xx}+\sigma_{xy})\tilde{\boldsymbol{a}}^u + (\sigma_{yy}+\sigma_{xy})\tilde{\boldsymbol{a}}^v]_{\hat{y}=(\alpha/L)-\hat{x}}\,\mathrm{d}\hat{x}\,\mathrm{d}z \tag{32a}$$

$$\tilde{\boldsymbol{m}}_M = \frac{\sqrt{2}}{2}s\int_{0^+}^{\alpha/L}\left[\hat{\mu}(\nu_x+\nu_y)(\nu_x\tilde{\boldsymbol{a}}^u+\nu_y\tilde{\boldsymbol{a}}^v)\right]_{\hat{y}=(\alpha/L)-\hat{x}}\mathrm{d}\hat{x} \tag{32b}$$

Similarly to the nonlinear contribution of the strain energy in Eq. (28), both of the expressions in Eq. (32) can be manipulated to extract their state-dependent portions and render their required spatial integrals time invariant. This procedure and its results are omitted for brevity, but can be found in [53].

F. Quadrant-Level Equations of In- and Out-of-Plane Motion

Using the time-varying generalization of the extended Hamilton's principle in Eq. (12), applying the standard Lagrangian mechanics formulation, and using the expansions in Eq. (15) and their derivatives, the discretized nonlinear EOM of the system are

$$\begin{aligned}&\left[\tilde{\boldsymbol{M}}_M+\tilde{\boldsymbol{M}}_B\right]\ddot{\boldsymbol{x}}+\left[\left(\dot{\tilde{\boldsymbol{M}}}_M+\dot{\tilde{\boldsymbol{M}}}_B\right)+\left(\tilde{\boldsymbol{G}}_M-\tilde{\boldsymbol{G}}_M^{\intercal}\right)+\left(\tilde{\boldsymbol{G}}_B-\tilde{\boldsymbol{G}}_B^{\intercal}\right)+\tilde{\boldsymbol{D}}\right]\dot{\boldsymbol{x}}\\&+\left[\tilde{\boldsymbol{k}}_{M,\mathrm{nln}}(\boldsymbol{x})+\tilde{\boldsymbol{k}}_{B,\mathrm{nln}}(\boldsymbol{x})\right]+\left[\left(\dot{\tilde{\boldsymbol{G}}}_M+\dot{\tilde{\boldsymbol{G}}}_B\right)-\left(\tilde{\boldsymbol{K}}_{M,T}+\tilde{\boldsymbol{K}}_{B,T}\right)\right.\\&\left.+\tilde{\boldsymbol{K}}_{B,U,2}\right]\boldsymbol{x}+\tilde{\boldsymbol{m}}_M(\boldsymbol{x},\dot{\boldsymbol{x}})+\tilde{\boldsymbol{w}}_M(\boldsymbol{x})+\dot{\tilde{\boldsymbol{\alpha}}}_M-\tilde{\boldsymbol{\beta}}_M=\boldsymbol{0}\end{aligned} \tag{33}$$

which can also be extended to a four-quadrant sail, as described in [21]. Compared against the linear EOM in [16], the nonlinear EOM in Eq. (33) of this paper involve nonlinear stiffness terms, $\tilde{\boldsymbol{k}}_{M,\mathrm{nln}}$ and $\tilde{\boldsymbol{k}}_{B,\mathrm{nln}}$, arising from the stresses and plate strains used to determine the strain energies in Eq. (14). In addition, the momentum transport and work terms in Eq. (12) result in $\tilde{\boldsymbol{m}}_M$ and $\tilde{\boldsymbol{w}}_M$, given by Eq. (32). Lastly, extra $\dot{\tilde{\boldsymbol{\alpha}}}_M$ and $\tilde{\boldsymbol{\beta}}_M$ terms are present, provided in Eqs. (21d) and (21e). These terms arise from the revisited kinetic energies in Eq. (14) and the modified velocity in Eq (13b). To make the model more realistic and in hopes of speeding up the simulations, a damping term of the form $\tilde{\boldsymbol{D}} = D(\tilde{\boldsymbol{M}}_M+\tilde{\boldsymbol{M}}_B)$ is also added, which, in some simulation cases, is necessary to avoid time integration failures, possibly arising from high-frequency oscillations. For some wrinkling studies, given that the interest is only in the steady-state shape, the proportionality constant D is increased to quickly eliminate the transient oscillations. Damping was also used in most of the simulations in [43].

G. Linear Algebraic Manipulations

The nonlinear state-dependent terms in Eq. (33) are problematic, in part because of the computational cost of reevaluating their spatial integrals at each time step, whereas updating the other matrices, with their transformed time-invariant integrals, simply involves multiplication by functions of $L(t)$ or its rates. To significantly improve efficiency, the following linear-algebra-based identities are developed and used to extract $\boldsymbol{x}$ and/or $\dot{\boldsymbol{x}}$ out of the nonlinear terms, such as $\tilde{\boldsymbol{k}}_{B,\mathrm{nln}}$ and $\tilde{\boldsymbol{k}}_{M,\mathrm{nln}}$, and have them multiply a time-invariant matrix from left and/or right:

$$(\boldsymbol{x}^{\intercal}\boldsymbol{s})\boldsymbol{t} = (\boldsymbol{t}\boldsymbol{s}^{\intercal})\boldsymbol{x} \tag{34a}$$

$$(\boldsymbol{x}^{\intercal}\boldsymbol{s})\boldsymbol{T}\boldsymbol{x} = \boldsymbol{X}^{\intercal}(\boldsymbol{T}_{\mathrm{row}}^{\intercal}\boldsymbol{s}^{\intercal})\boldsymbol{x} \tag{34b}$$

$$(\boldsymbol{x}^{\intercal}\boldsymbol{S}\boldsymbol{x})\boldsymbol{t} = (\boldsymbol{t}\boldsymbol{S}_{\mathrm{col}}^{\intercal})\boldsymbol{X}\boldsymbol{x} \tag{34c}$$

$$(\boldsymbol{x}^{\intercal}\boldsymbol{S}\boldsymbol{x})\boldsymbol{T}\boldsymbol{x} = \boldsymbol{X}^{\intercal}(\boldsymbol{T}_{\mathrm{row}}^{\intercal}\boldsymbol{S}_{\mathrm{col}}^{\intercal})\boldsymbol{X}\boldsymbol{x} \tag{34d}$$

where $\boldsymbol{x}$, which can be replaced by $\dot{\boldsymbol{x}}$, is a time-dependent $n\times 1$ matrix, $\boldsymbol{s}$ and $\boldsymbol{t}$ are generic space-dependent $n\times 1$ matrices; whereas $\boldsymbol{S}$ and $\boldsymbol{T}$ are generic space-dependent $n\times n$ matrices. In addition, $\boldsymbol{S}_{\mathrm{col}} \triangleq [\boldsymbol{S}^{1\intercal}\ \cdots\ \boldsymbol{S}^{n\intercal}]^{\intercal}$ is a column matrix of the columns of $\boldsymbol{S}$, and $\boldsymbol{T}_{\mathrm{row}} \triangleq [\boldsymbol{T}_1\ \cdots\ \boldsymbol{T}_n]$ is a row matrix of the rows of $\boldsymbol{T}$. Lastly, $\boldsymbol{X} \triangleq \mathrm{blockdiag}\{\boldsymbol{x},\ldots,\boldsymbol{x}\}$.

If $\boldsymbol{x}$ is set to be the generalized coordinates of Eq. (15), the spatial integration of the expressions on the left-hand side of Eq. (34) needs to keep $\boldsymbol{x}(t)$ within the integrals: for example, $\boldsymbol{s}\boldsymbol{T}$ is dimensionally not valid. However, the right-hand side that has time-invariant matrices sandwiched between functions of $\boldsymbol{x}(t)$ can have such functions moved out. Although the required matrices can grow as large as proportionally to n^4, they are sparse and eliminate the need for reintegration at each time step. For example, the time integration of a test case would take about 40 h using the symbolic implementation, but transformations of this section reduced the same integration to about 30 min, at the one-time overhead cost of computing and storing the spatial integrals (possibly up to a few days for a large n).

All the stress and strain expressions in Eqs. (25–27) are in the following form:

$$\sigma_{ij} = \boldsymbol{x}^{\intercal}\boldsymbol{s}_{ij} + \frac{1}{2}\boldsymbol{x}^{\intercal}\boldsymbol{S}_{ij}\boldsymbol{x}, \quad \boldsymbol{s}_{ij} \triangleq \boldsymbol{s}_{ij,1}(x,y,L) + \boldsymbol{s}_{ij,2}(x,y,z,L^2) \tag{35a}$$

$$\epsilon_{ij} = \boldsymbol{x}^{\intercal}\boldsymbol{t}_{ij} + \frac{1}{2}\boldsymbol{x}^{\intercal}\boldsymbol{T}_{ij}\boldsymbol{x}, \quad \boldsymbol{t}_{ij} \triangleq \boldsymbol{t}_{ij,1}(x,y,L) + \boldsymbol{t}_{ij,2}(x,y,z,L^2) \tag{35b}$$

where the subscript ij belongs to $\{xx, yy, xy\}$, and the coefficients $\boldsymbol{s}$, $\boldsymbol{t}$, $\boldsymbol{S}$, and $\boldsymbol{T}$ are state independent but time dependent [owing to $L(t)$]. Therefore, expressions similar to the following (for each direction) appear as part of the nonlinear membrane strain term, $\tilde{\boldsymbol{k}}_{M,\mathrm{nln}}$, in Eq. (28a):

$$\begin{aligned}\frac{\partial}{\partial\boldsymbol{x}}(\sigma_{ij}\epsilon_{ij}) = &\left(\boldsymbol{x}^{\intercal}\boldsymbol{s}_{ij}+\frac{1}{2}\boldsymbol{x}^{\intercal}\boldsymbol{S}_{ij}\boldsymbol{x}\right)(\boldsymbol{t}_{ij}+\boldsymbol{T}_{ij}\boldsymbol{x})\\&+\left(\boldsymbol{x}^{\intercal}\boldsymbol{t}_{ij}+\frac{1}{2}\boldsymbol{x}^{\intercal}\boldsymbol{T}_{ij}\boldsymbol{x}\right)(\boldsymbol{s}_{ij}+\boldsymbol{S}_{ij}\boldsymbol{x})\end{aligned} \tag{36}$$

to all terms of which the expressions in Eq. (34) are applicable. More specifically, focusing on the stress terms of the taut regions in Eq. (26) and the strains as written in Eq. (25), the following state-independent coefficients correspond to the forms in Eq. (35):

$$\begin{aligned}&\sigma_{T,xx}\colon \boldsymbol{s}_{xx,1} \triangleq \frac{C_1}{L}\left(\tilde{\boldsymbol{a}}^u_{,\hat{x}}+\nu\tilde{\boldsymbol{a}}^v_{,\hat{y}}\right), \quad \boldsymbol{s}_{xx,2} \triangleq \frac{-C_1 z}{L^2}\left(\tilde{\boldsymbol{a}}^w_{,\hat{x}\hat{x}}+\nu\tilde{\boldsymbol{a}}^w_{,\hat{y}\hat{y}}\right),\\&\qquad \boldsymbol{S}_{xx} \triangleq \frac{C_1}{L^2}\left(\tilde{\boldsymbol{a}}^w_{,\hat{x}}\tilde{\boldsymbol{a}}^{w\intercal}_{,\hat{x}}+\nu\tilde{\boldsymbol{a}}^w_{,\hat{y}}\tilde{\boldsymbol{a}}^{w\intercal}_{,\hat{y}}\right)\\&\epsilon_{xx}\colon \boldsymbol{t}_{xx,1} \triangleq \frac{1}{L}\tilde{\boldsymbol{a}}^u_{,\hat{x}}, \quad \boldsymbol{t}_{xx,2} \triangleq \frac{-z}{L^2}\tilde{\boldsymbol{a}}^w_{,\hat{x}\hat{x}}, \quad \boldsymbol{T}_{xx} \triangleq \frac{1}{L^2}\tilde{\boldsymbol{a}}^w_{,\hat{x}}\tilde{\boldsymbol{a}}^{w\intercal}_{,\hat{x}}\end{aligned} \tag{37a}$$

$$\begin{aligned}&\sigma_{T,yy}\colon \boldsymbol{s}_{yy,1} \triangleq \frac{C_1}{L}\left(\nu\tilde{\boldsymbol{a}}^u_{,\hat{x}}+\tilde{\boldsymbol{a}}^v_{,\hat{y}}\right), \quad \boldsymbol{s}_{yy,2} \triangleq \frac{-C_1 z}{L^2}\left(\nu\tilde{\boldsymbol{a}}^w_{,\hat{x}\hat{x}}+\tilde{\boldsymbol{a}}^w_{,\hat{y}\hat{y}}\right),\\&\qquad \boldsymbol{S}_{yy} \triangleq \frac{C_1}{L^2}\left(\nu\tilde{\boldsymbol{a}}^w_{,\hat{x}}\tilde{\boldsymbol{a}}^{w\intercal}_{,\hat{x}}+\tilde{\boldsymbol{a}}^w_{,\hat{y}}\tilde{\boldsymbol{a}}^{w\intercal}_{,\hat{y}}\right)\\&\epsilon_{yy}\colon \boldsymbol{t}_{yy,1} \triangleq \frac{1}{L}\tilde{\boldsymbol{a}}^v_{,\hat{y}}, \quad \boldsymbol{t}_{yy,2} \triangleq \frac{-z}{L^2}\tilde{\boldsymbol{a}}^w_{,\hat{y}\hat{y}}, \quad \boldsymbol{T}_{yy} \triangleq \frac{1}{L^2}\tilde{\boldsymbol{a}}^w_{,\hat{y}}\tilde{\boldsymbol{a}}^{w\intercal}_{,\hat{y}}\end{aligned} \tag{37b}$$

$$\sigma_{T,xy}\colon \boldsymbol{s}_{xy,1} \triangleq \frac{C_2}{L}\left(\frac{1}{2}(\tilde{\boldsymbol{a}}^{u}_{,\hat{y}} + \tilde{\boldsymbol{a}}^{v}_{,\hat{x}})\right), \quad \boldsymbol{s}_{xy,2} \triangleq \frac{-C_2 z}{L^2}\tilde{\boldsymbol{a}}^{w}_{,\hat{x}\hat{y}},$$
$$\boldsymbol{S}_{xy} \triangleq \frac{C_2}{L^2}\tilde{\boldsymbol{a}}^{w}_{,\hat{x}}\tilde{\boldsymbol{a}}^{w\intercal}_{,\hat{y}}$$
$$\epsilon_{xy}\colon \boldsymbol{t}_{xy,1} \triangleq \frac{1}{L}\left(\frac{1}{2}(\tilde{\boldsymbol{a}}^{u}_{,\hat{y}} + \tilde{\boldsymbol{a}}^{v}_{,\hat{x}})\right), \quad \boldsymbol{t}_{xy,2} \triangleq \frac{-z}{L^2}\tilde{\boldsymbol{a}}^{w}_{,\hat{x}\hat{y}},$$
$$\boldsymbol{T}_{xy} \triangleq \frac{1}{L^2}\tilde{\boldsymbol{a}}^{w}_{,\hat{x}}\tilde{\boldsymbol{a}}^{w\intercal}_{,\hat{y}} \tag{37c}$$

where $C_1 \triangleq E/(1-\nu^2)$ and $C_2 \triangleq E/(1+\nu)$ are constants. Lastly, upon extracting the time-varying $L(t)$ from the aforementioned coefficients and using Eq. (36) for each direction along with the identities in Eq. (34), the following expression is obtained for the integrand of the derivative of the membrane strain energy in the taut regions, $\partial\hat{\mathcal{U}}_{M,T}/\partial\boldsymbol{x}$, to be triple integrated in all directions, as in Eq. (28a), to appear as part of the nonlinear membrane strain term, $\tilde{\boldsymbol{k}}_{M,\mathrm{nln}}$, in the EOM in Eq. (33):

$$\begin{aligned}\frac{\partial}{\partial\boldsymbol{x}}\left(\frac{1}{2}\sum_{\{i,j\}}^{\{x,y\}}\sigma_{T,ij}\epsilon_{ij}\right) = \frac{1}{2}\sum_{\{i,j\}}^{\{x,y\}}\Bigg\{&\sum_{p=1}^{2}\sum_{q=1}^{2}\frac{1}{L^{p+q}}\left[\hat{\boldsymbol{t}}_{ij,p}\hat{\boldsymbol{s}}^{\intercal}_{ij,q} + \hat{\boldsymbol{s}}_{ij,p}\hat{\boldsymbol{t}}^{\intercal}_{ij,q}\right]\boldsymbol{x}\\ &+ \sum_{p=1}^{2}\frac{1}{L^{2+p}}\boldsymbol{X}^{\intercal}\left[\hat{\boldsymbol{T}}^{\intercal}_{\mathrm{row},ij}\hat{\boldsymbol{s}}^{\intercal}_{ij,p} + \hat{\boldsymbol{S}}^{\intercal}_{\mathrm{row},ij}\hat{\boldsymbol{t}}^{\intercal}_{ij,p}\right]\boldsymbol{x}\\ &+ \sum_{p=1}^{2}\frac{1}{2L^{2+p}}\left[\hat{\boldsymbol{t}}_{ij,p}\hat{\boldsymbol{S}}^{\intercal}_{\mathrm{col},ij} + \hat{\boldsymbol{s}}_{ij,p}\hat{\boldsymbol{T}}^{\intercal}_{\mathrm{col},ij}\right]\boldsymbol{X}\boldsymbol{x}\\ &+ \frac{1}{2L^4}\boldsymbol{X}^{\intercal}\left[\hat{\boldsymbol{T}}^{\intercal}_{\mathrm{row},ij}\hat{\boldsymbol{S}}^{\intercal}_{\mathrm{col},ij} + \hat{\boldsymbol{S}}^{\intercal}_{\mathrm{row},ij}\hat{\boldsymbol{T}}^{\intercal}_{\mathrm{col},ij}\right]\boldsymbol{X}\boldsymbol{x}\Bigg\}\end{aligned} \tag{38}$$

where $\sum_{\{i,j\}}^{\{x,y\}}$ indicates summation over the subscripted variables corresponding to the different directions, namely, $\{xx, yy, xy, yx\}$, with the variables of the last two subscripts being identical. In addition, the hatted coefficients are the L-extracted equivalents of those in Eq. (37): for example, $\boldsymbol{s}_{xx,p} = \hat{\boldsymbol{s}}_{xx,p}/L^p$ and $\boldsymbol{S}_{xx} = \hat{\boldsymbol{S}}_{xx}/L^2$. The required spatial integration now need be performed only once, before the time integration begins, on the terms enclosed in square brackets.

Similar manipulations are applicable to the wrinkled regions, governed by the stresses in Eq. (27). However, owing to the presence of the time-varying $Q(t)$ and $R(t)$ coefficients in Eq. (8), which in turn depend on the averaged principal strains in each mesh region, more coefficients are required to allow for removing the time dependence from the required integrals. The following state-independent coefficients correspond to the σ forms in Eq. (35a), whereas the $\boldsymbol{t}$ and $\boldsymbol{T}$ coefficients used for the strains are still applicable, as provided in Eq. (37):

where $Q(t)$ and $R(t)$ are state dependent and change over time, because of which the variables they are multiplied with are separated to form, via addition, $\boldsymbol{s}_{1,1} + \boldsymbol{s}_{2,1} = \boldsymbol{s}_1(x, y, L)$, $\boldsymbol{s}_{1,2} + \boldsymbol{s}_{2,2} = \boldsymbol{s}_2(x, y, z, L^2)$, and $\boldsymbol{S}_1 + \boldsymbol{S}_2 = \boldsymbol{S}(x, y, L^2)$ of the general form in Eq. (35a). Upon extracting $Q(t)$, $R(t)$, and $L(t)$ from the aforementioned coefficients and using Eq. (36) for each direction along with the identities in Eq. (34), the following expression is obtained for the integrand of the derivative of the membrane strain energy in the wrinkled regions, $\partial\hat{\mathcal{U}}_{M,W}/\partial\boldsymbol{x}$, to be triple integrated in all directions, as in Eq. (28a), to appear as part of the nonlinear strain term, $\tilde{\boldsymbol{k}}_{M,\mathrm{nln}}$, in the EOM in Eq. (33):

$$\begin{aligned}&\frac{\partial}{\partial\boldsymbol{x}}\left(\frac{1}{2}\sum_{\{i,j\}}^{\{x,y\}}\sigma_{W,ij}\epsilon_{ij}\right)\\ &= \frac{1}{2}\sum_{\{i,j\}}^{\{x,y\}}\Bigg\{\sum_{r=1}^{2}\sum_{p=1}^{2}\sum_{q=1}^{2}\frac{\kappa_{ij,r}}{L^{p+q}}\left[\hat{\boldsymbol{t}}_{ij,p}\hat{\boldsymbol{s}}^{\intercal}_{ij,r,q} + \hat{\boldsymbol{s}}_{ij,r,p}\hat{\boldsymbol{t}}^{\intercal}_{ij,q}\right]\boldsymbol{x}\\ &\quad+ \sum_{r=1}^{2}\sum_{p=1}^{2}\frac{\kappa_{ij,r}}{L^{2+p}}\boldsymbol{X}^{\intercal}\left[\hat{\boldsymbol{T}}^{\intercal}_{\mathrm{row},ij}\hat{\boldsymbol{s}}^{\intercal}_{ij,r,p} + \hat{\boldsymbol{S}}^{\intercal}_{\mathrm{row},ij,r}\hat{\boldsymbol{t}}^{\intercal}_{ij,p}\right]\boldsymbol{x}\\ &\quad+ \sum_{r=1}^{2}\sum_{p=1}^{2}\frac{\kappa_{ij,r}}{2L^{2+p}}\left[\hat{\boldsymbol{t}}_{ij,p}\hat{\boldsymbol{S}}^{\intercal}_{\mathrm{col},ij,r} + \hat{\boldsymbol{s}}_{ij,r,p}\hat{\boldsymbol{T}}^{\intercal}_{\mathrm{col},ij}\right]\boldsymbol{X}\boldsymbol{x}\\ &\quad+ \sum_{r=1}^{2}\frac{\kappa_{ij,r}}{2L^4}\boldsymbol{X}\hat{\boldsymbol{T}}\left[\hat{\boldsymbol{T}}^{\intercal}_{\mathrm{row},ij}\hat{\boldsymbol{S}}^{\intercal}_{\mathrm{col},ij,r} + \hat{\boldsymbol{S}}^{\intercal}_{\mathrm{row},ij,r}\hat{\boldsymbol{T}}^{\intercal}_{\mathrm{col},ij}\right]\boldsymbol{X}\boldsymbol{x}\Bigg\}\end{aligned} \tag{40}$$

where the notation is the same as that used in Eq. (38), with the exception of the new subscript, r, to distinguish between the first and second rows of the new (wrinkled) coefficients in Eq. (39). Also extra are the following $\kappa_{ij,r}$ coefficients based on Eq. (39):

$$\sigma_{W,xx}\colon\ \kappa_{xx,1} \triangleq 1 + R, \quad \kappa_{xx,2} \triangleq Q \tag{41a}$$

$$\sigma_{W,yy}\colon\ \kappa_{yy,1} \triangleq 1 - R, \quad \kappa_{yy,2} \triangleq Q \tag{41b}$$

$$\sigma_{W,xy}\colon\ \kappa_{xy,1} \triangleq Q, \qquad \kappa_{xy,2} \triangleq 1 \tag{41c}$$

The required spatial integration now need be performed only once, before the time integration begins, on the terms of Eq. (40) enclosed in square brackets.

Lastly, similar operations can be performed on the nonlinear portion of the strain energy of the booms, $\tilde{\boldsymbol{k}}_{B,\mathrm{nln}}$ in Eq. (28b), as well as the boundary work and momentum transfer terms, $\tilde{\boldsymbol{w}}_M$ and $\tilde{\boldsymbol{m}}_M$ in Eq. (32). The details of those operations and their results are omitted, but can be found in [53].

$$\sigma_{W,xx}\colon\ \boldsymbol{s}_{xx,1,1} \triangleq (1+R)\frac{E}{4L}(2\tilde{\boldsymbol{a}}^{u}_{,\hat{x}}), \quad \boldsymbol{s}_{xx,1,2} \triangleq (1+R)\frac{-Ez}{4L^2}(2\tilde{\boldsymbol{a}}^{w}_{,\hat{x}\hat{x}}), \quad \boldsymbol{S}_{xx,1} \triangleq (1+R)\frac{E}{4L^2}(2\tilde{\boldsymbol{a}}^{w}_{,\hat{x}}\tilde{\boldsymbol{a}}^{w\intercal}_{,\hat{x}})$$
$$\boldsymbol{s}_{xx,2,1} \triangleq Q\frac{E}{4L}(\tilde{\boldsymbol{a}}^{u}_{,\hat{y}} + \tilde{\boldsymbol{a}}^{v}_{,\hat{x}}), \quad \boldsymbol{s}_{xx,2,2} \triangleq Q\frac{-Ez}{4L^2}(2\tilde{\boldsymbol{a}}^{w}_{,\hat{x}\hat{y}}), \quad \boldsymbol{S}_{xx,2} \triangleq Q\frac{E}{4L^2}(2\tilde{\boldsymbol{a}}^{w}_{,\hat{x}}\tilde{\boldsymbol{a}}^{w\intercal}_{,\hat{y}}) \tag{39a}$$

$$\sigma_{W,yy}\colon\ \boldsymbol{s}_{yy,1,1} \triangleq (1-R)\frac{E}{4L}(2\tilde{\boldsymbol{a}}^{v}_{,\hat{y}}), \quad \boldsymbol{s}_{yy,1,2} \triangleq (1-R)\frac{-Ez}{4L^2}(2\tilde{\boldsymbol{a}}^{w}_{,\hat{y}\hat{y}}), \quad \boldsymbol{S}_{yy,1} \triangleq (1-R)\frac{E}{4L^2}(2\tilde{\boldsymbol{a}}^{w}_{,\hat{y}}\tilde{\boldsymbol{a}}^{w\intercal}_{,\hat{y}})$$
$$\boldsymbol{s}_{yy,2,1} \triangleq Q\frac{E}{4L}(\tilde{\boldsymbol{a}}^{u}_{,\hat{y}} + \tilde{\boldsymbol{a}}^{v}_{,\hat{x}}), \quad \boldsymbol{s}_{yy,2,2} \triangleq Q\frac{-Ez}{4L^2}(2\tilde{\boldsymbol{a}}^{w}_{,\hat{x}\hat{y}}), \quad \boldsymbol{S}_{yy,2} \triangleq Q\frac{E}{4L^2}(2\tilde{\boldsymbol{a}}^{w}_{,\hat{x}}\tilde{\boldsymbol{a}}^{w\intercal}_{,\hat{y}}) \tag{39b}$$

$$\sigma_{W,xy}\colon\ \boldsymbol{s}_{xy,1,1} \triangleq Q\frac{E}{4L}(\tilde{\boldsymbol{a}}^{u}_{,\hat{x}} + \tilde{\boldsymbol{a}}^{v}_{,\hat{y}}), \quad \boldsymbol{s}_{xy,1,2} \triangleq Q\frac{-Ez}{4L^2}(\tilde{\boldsymbol{a}}^{w}_{,\hat{x}\hat{x}} + \tilde{\boldsymbol{a}}^{w}_{,\hat{y}\hat{y}}), \quad \boldsymbol{S}_{xy,1} \triangleq Q\frac{E}{4L^2}(\tilde{\boldsymbol{a}}^{w}_{,\hat{x}}\tilde{\boldsymbol{a}}^{w\intercal}_{,\hat{x}} + \tilde{\boldsymbol{a}}^{w}_{,\hat{y}}\tilde{\boldsymbol{a}}^{w\intercal}_{,\hat{y}})$$
$$\boldsymbol{s}_{xy,2,1} \triangleq \frac{E}{4L}(\tilde{\boldsymbol{a}}^{u}_{,\hat{y}} + \tilde{\boldsymbol{a}}^{v}_{,\hat{x}}), \quad \boldsymbol{s}_{xy,2,2} \triangleq \frac{-Ez}{4L^2}(2\tilde{\boldsymbol{a}}^{w}_{,\hat{x}\hat{y}}), \quad \boldsymbol{S}_{xy,2} \triangleq \frac{E}{4L^2}(2\tilde{\boldsymbol{a}}^{w}_{,\hat{x}}\tilde{\boldsymbol{a}}^{w\intercal}_{,\hat{y}}) \tag{39c}$$

IV. Wrinkling Study

The approach for wrinkling predictions involves using a coarse mesh (shown in Fig. 2) while maintaining the global expansions for the deflections and continuously adjusting the constitutive relation based on the wrinkling state in each region. The number of regions is controlled by setting how many elements, K, each boom is divided into. The state of each element is determined using the wrinkling criterion in Eq. (7), and the appropriate local elasticity matrix is selected based on Eq. (8).

For a static problem, an iteration would be required: using an initial guess for each local $\boldsymbol{C}$ based on the previous strain state, obtaining revised stress estimates and checking their compatibility against the initial guess, revising $\boldsymbol{C}$ based on the updated strains, and repeating until convergence [39]. This may not be needed for dynamic problems, given their nonequilibrium nature and that continuous load and stress changes alleviate the need for a converged solution, and even when it was adopted in this work, convergence was achieved within one or two iterations.

Consider the mesh shown in Fig. 2, with triangular elements of base length $d = L/K$. If an integral over the entire membrane quadrant is required and the integrand depends on the mesh elements, as is the case for the nonlinear terms in the previous section that are computed using the local stress/strain values, the result should be evaluated by breaking the integral into element-wise subintegrals. For the light-colored upright elements in Fig. 2, labeled 1 to 6, the subintegrals are

$$k=1:\int_{0^+}^{d}\int_{0^+}^{d-x}(\cdot)\,\mathrm{d}y\,\mathrm{d}x,\quad k=2:\int_{d}^{2d}\int_{0^+}^{2d-x}(\cdot)\,\mathrm{d}y\,\mathrm{d}x,\ \cdots,$$
$$k=6:\int_{0^+}^{d}\int_{2d}^{3d-x}(\cdot)\,\mathrm{d}y\,\mathrm{d}x \tag{42}$$

which can all be written using the coordinates of corners 1, 2, and 3 of the elements, also labeled in Fig. 2, as

$$\text{Element } k:\int_{x_{1,k}}^{x_{2,k}}\int_{y_{2,k}=y_{1,k}}^{(x_{3,k}+y_{3,k})-x}(\cdot)\,\mathrm{d}y\,\mathrm{d}x \tag{43}$$

with the corner coordinates generated by

$$(x_1,y_1)=(i,j)\times d,\quad (x_2,y_2)=(i+1,j)\times d,$$
$$(x_3,y_3)=(i,j+1)\times d \tag{44}$$

using a nested loop with $j\in\{0,\ldots,K-1\}$ and $i\in\{0,\ldots,(K-1)-j\}$, where K is the number of elements on each boom. Similarly, for the dark-colored upside-down elements in Fig. 2, labeled 7 to 9, the subintegrals are

$$k=7:\int_{0^+}^{d}\int_{d-x}^{d}(\cdot)\,\mathrm{d}y\,\mathrm{d}x,\quad k=8:\int_{d}^{2d}\int_{2d-x}^{d}(\cdot)\,\mathrm{d}y\,\mathrm{d}x,$$
$$k=9:\int_{0^+}^{d}\int_{2d-x}^{2d}(\cdot)\,\mathrm{d}y\,\mathrm{d}x \tag{45}$$

which can all be written using the corner coordinates of the elements as

$$\text{Element } k:\int_{x_{2,k}}^{x_{1,k}}\int_{(x_{3,k}+y_{3,k})-x}^{y_{2,k}=y_{1,k}}(\cdot)\,\mathrm{d}y\,\mathrm{d}x=\int_{x_{1,k}}^{x_{2,k}}\int_{y_{2,k}=y_{1,k}}^{(x_{3,k}+y_{3,k})-x}(\cdot)\,\mathrm{d}y\,\mathrm{d}x \tag{46}$$

with the corner coordinates generated by

$$(x_1,y_1)=(i,j)\times d,\quad (x_2,y_2)=(i-1,j)\times d,$$
$$(x_3,y_3)=(i,j-1)\times d \tag{47}$$

using a nested loop with $j\in\{1,\ldots,K-1\}$ and $i\in\{1,\ldots,K-j\}$. The expression in Eq. (46) is the same as that in Eq. (43), providing a uniform expression applicable to all mesh elements that lends itself well to numerical implementation. With this formulation, the updated strain energy of membrane (ab) in Eq. (14a) becomes

$$\mathcal{U}_{M,ab}=\sum_{k=1}^{K^2}\int_{x_{1,k}}^{x_{2,k}}\int_{y_{2,k}=y_{1,k}}^{(x_{3,k}+y_{3,k})-x}\int_{-s/2}^{s/2}\frac{1}{2}\boldsymbol{\sigma}^{\mathsf{T}}\epsilon\,\mathrm{d}z\,\mathrm{d}y\,\mathrm{d}x \tag{48}$$

where the local integration bounds, $x_{i,k}$ and $y_{i,k}$, denote the coordinates of the corners of the kth mesh element, as labeled in Fig. 2. To determine $\boldsymbol{\sigma}$, the appropriate local elasticity matrix in Eq. (8) is used, for which averaged strains are obtained using a finite number of representative points, shown as crosses within the elements in Fig. 2. Note also the need for integration over the thickness s, because of the z dependence of the plate strain terms in Eq. (6). Because the mesh elements are independent, the mesh-dependent spatial integrations can be performed in parallel, using MATLAB®'s Parallel Computing toolbox, for example.

The membrane kinetic energy $\mathcal{T}_{M,ab}$ remains the same as that in Eq. (14a), and the expressions for the boom energies remain the same as those in Eq. (14b). As for the outlet work and momentum transfer expressions, after applying the mesh and assuming it is coarse enough that the entire outlet is contained within its first element, $k=1$, we have the same expressions as those in Eq. (32), but using the wrinkling state and corresponding stresses of the $k=1$ mesh element.

V. Results

Numerical simulations are performed by integrating the nonlinear dynamics EOM in Eq. (33). First, a concise overview of the simulation procedure and parameters used is provided. Then, the convergence of the predicted wrinkling model in response to mesh refinement is examined using a deploying quadrant. The response of a quadrant to nonzero initial conditions (ICs) under a constant-rate deployment profile is subsequently studied using a coarse mesh by focusing on the major principal stresses, wrinkled regions, and their evolution over time. The results obtained using the nonlinear model of this study are also compared against those using the linear model of Vatankhahghadim and Damaren [16] in the same deployment scenario, upon setting the ICs in a way that reproduces the initial stress distribution assumed by the Airy stress function of the linear model, but only at the initial time $t_0=0$. Lastly, a comparison of the results against earlier simulations, in turn validated experimentally, using a constant-size loaded membrane is also made at the end of this section.

A. Simulation Procedure and Parameters

Even though the EOM involve system matrices that are time varying (for deployment with nonzero $\dot{L}$), the coordinate transformations and the linear algebraic manipulations described in the previous section render all the required space integrals time invariant. The simulation procedure starts by constructing all the necessary integrands and evaluating the spatial integrals required for the system matrices. The results of these integrals can then be stored and reused in future simulations that use the same sail parameters. Then, numerical time integration of the EOM is performed, at each time step of which the system matrices are evaluated via multiplying the precalculated spatial integrals by the remaining functions of $L(t)$, $\boldsymbol{x}(t)$, and their rates.

To perform the previously described wrinkling predictions, before evaluating the system matrices the wrinkling state at each time step is first determined using the wrinkling criterion in Eq. (7). Then, depending on the state of each mesh element, either the taut or the wrinkled constitutive relation is used to determine the contribution of the element to each of the system matrices that depend on the stresses and strains. These column matrices are the nonlinear stiffness terms, $\tilde{\boldsymbol{k}}_{B,\mathrm{nln}}$ and $\tilde{\boldsymbol{k}}_{M,\mathrm{nln}}$, as well as the work on the outlet $\tilde{\boldsymbol{w}}_M$.

The simulations use MATLAB's built-in variable-step-size ode15s() with relative and absolute error tolerances of 'RelTol' $=10^{-4}$ and 'AbsTol' $=10^{-6}$, respectively. Table 1 lists the physical and geometric properties that are assumed for most of the simulations, unless otherwise stated in each subsection. Other than the variable membrane

Table 1 Physical and geometric parameters assumed, unless otherwise stated, for the solar sail quadrant

Booms		Membranes	
E, N/m^2	2.87×10^{10}	E, N/m^2	4.00×10^{9}
A, m^2	1.61×10^{-5}	ν	0.3
I, m^4	8.05×10^{-8}	s , m	1×10^{-5}
ρ, kg/m	2.32×10^{-2}	μ , kg/m^2	Variable

density, $\mu(x, y)$, these values match those used in [43], halved when needed (for A, I, and ρ) to account for the quadrant nature of the test cases, which are in turn based on the previously reported results and experiments, with the membrane properties similar to those of Kapton®. For the interface through which mass flow occurs, assumed to have the linear shape in Fig. 3b, a distance of $\alpha/L = 10^{-4}$ is used.

B. Convergence of Wrinkling States with Mesh Refinement

A mesh refinement study is conducted using short simulations of the dynamics of a quadrant with most of the same parameters as those in Table 1, but with $v = 0.9$, to increase the coupling between the in-plane and out-of-plane dynamics, a choice that will be later made and justified when comparing the results to those of the linear model as well. The deployment profile is set to $L(t) = 50 + 0.1t$ m, and given the small duration of the simulation (only 0.01 s) and the nearly fully deployed nature of the sail, a uniform density of $\mu(x, y) = \mu_{\text{uni}} = 1.39 \times 10^{-2}$ kg/m^2 is assumed. The numbers of boom and membrane quasi modes used are $n_B = 2$ and $n_M = 4$, and the ICs are all set to zero except $\boldsymbol{p}_a(0) = \boldsymbol{p}_b(0) = [1\ 0]^{\intercal}/[5L(0)]$ and $\boldsymbol{e}_a(0) = \boldsymbol{e}_b(0) = 10^{-2} \times [1\ 0]^{\intercal}/[5L(0)]$, which are symmetric and used to also check the symmetry of the results, resulting in the small initial out-of- and in-plane deflections of the boom tips of -8 and -0.08 mm, respectively. Structural damping with a coefficient of $D = 1$ is added. Note that this does not imply critical damping, because D is not the effective damping ratio of the structure.

The purpose of this study was to determine whether the wrinkling states in each sail region are predicted more or less consistently as the mesh is refined. Shown in Figs. 4 and 5 are the predicted states at two instances, halfway and end, respectively, of a 0.01 s simulation. The number of mesh elements per boom is increased from $K = 2$ to $K = 5$ in each figure. Symmetry is maintained in all cases, as expected. As for the predicted patterns, all the meshes show complete wrinkling throughout the sail at $t = 0.005$ s in Fig. 4. As time progresses, the $K = 2$ case in Fig. 5a proves to be too coarse to capture any of the slack regions; however, the rest of the cases all do capture the overall taut–slack–wrinkled pattern, although the $K = 3$ mesh in Fig. 5b does not have sufficient elements to detect the small wrinkled region close to the origin. This is to be expected from the limitations of a coarser mesh, and at the same, too fine of a mesh will conflict with the global expansion-based approach adopted in this project. Overall, the results are deemed to be more or less consistent, and the fact that there are no surprise changes as a consequence of mesh refinement is promising in terms of the convergence of the model.

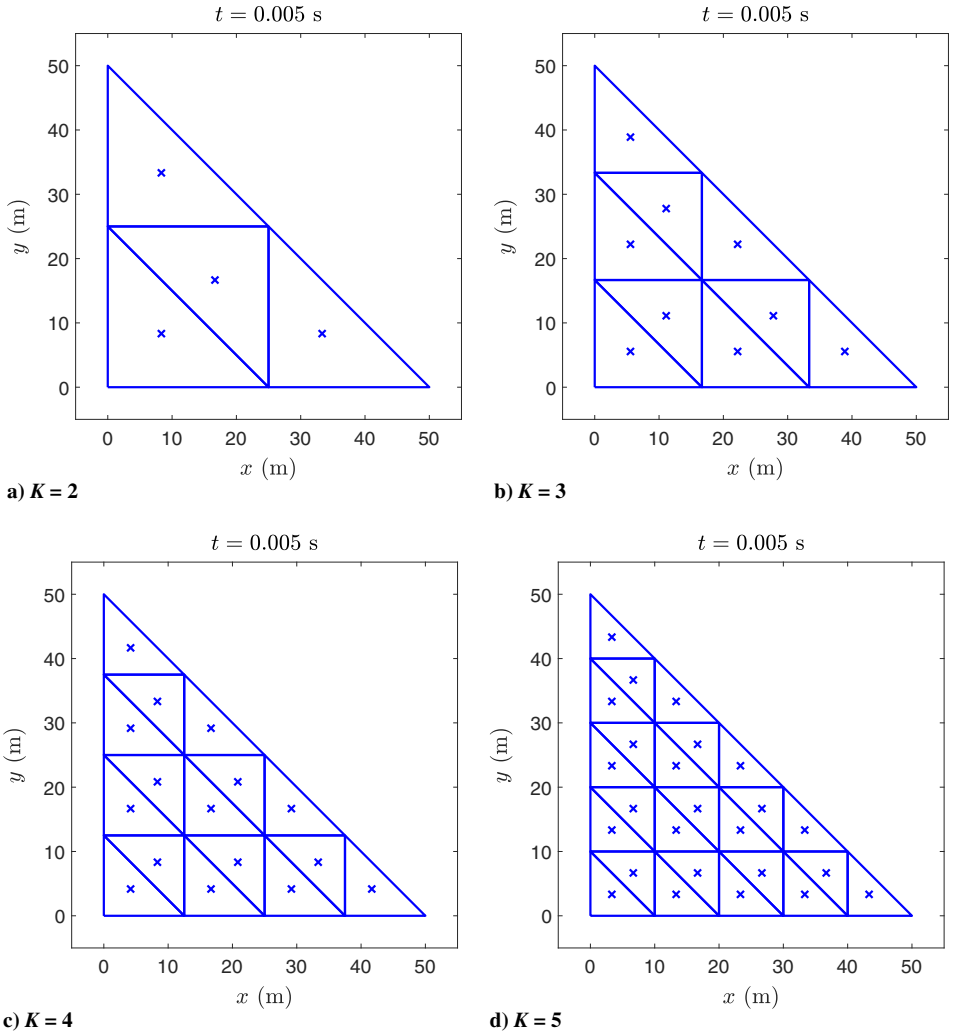

Fig. 4 Wrinkling states: cross (×) for wrinkled, at $t = 0.005$ s in the deploying quadrant of Subsection B, with different numbers K of mesh elements per boom.

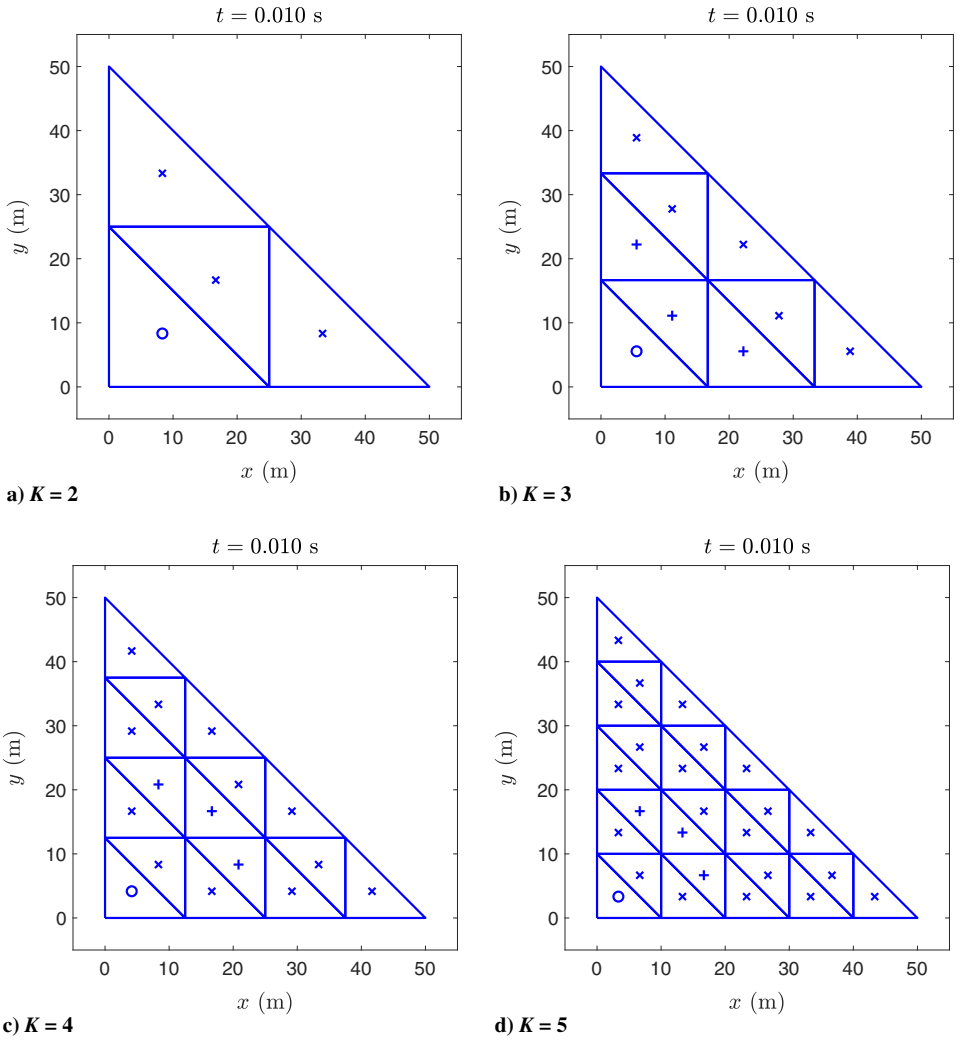

Fig. 5 Wrinkling states: circle (○) for taut, cross (×) for wrinkled, and plus (+) for slack, at $t = 0.01$ s in the deploying quadrant of Subsection B, with different numbers K of mesh elements per boom.

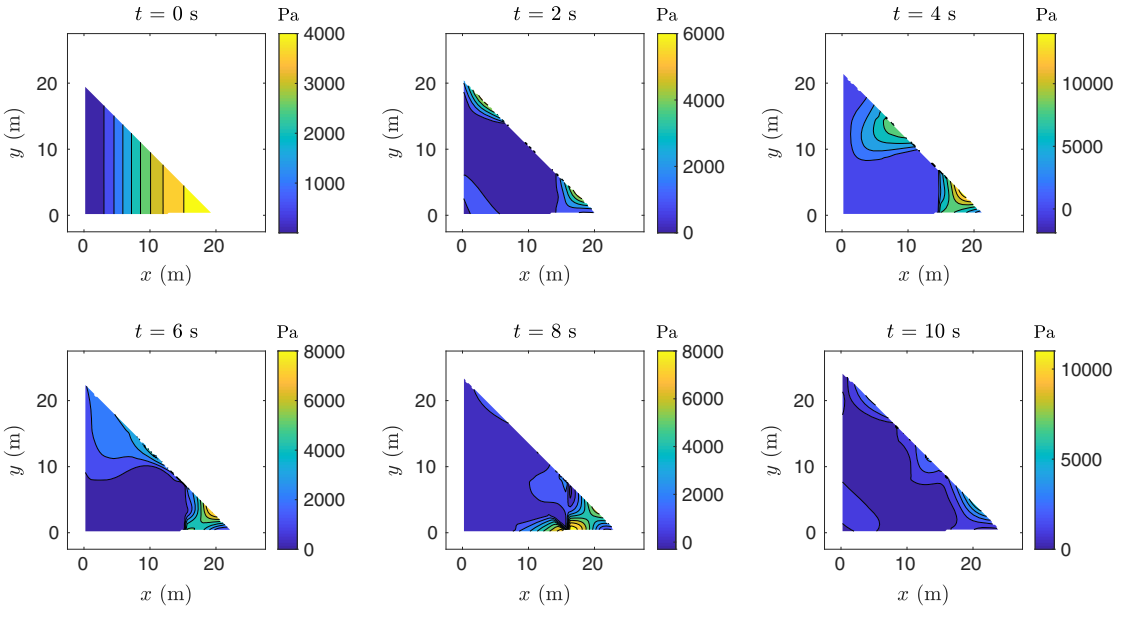

Fig. 6 Major principal stresses in the deploying quadrant of Subsection C.

C. Stress and Wrinkling of the Deploying Quadrant

The response of a sail quadrant to nonzero ICs under a constant-rate deployment profile is studied in this section by offering crude predictions, using a coarse mesh, of the major principal stresses, wrinkled regions, and their evolution over time. The numbers of boom and membrane quasi modes are set to $n_B = 2$ and $n_M = 4$, respectively. The parameters in Table 1 are selected. The density profile in Eq. (2) is used, with $\mu_c = 50\mu_{\text{uni}} = 50(1.39 \times 10^{-2})$ kg/m^2 and $\hat{c} = 0.01$. The ICs of boom (a) are set to $\boldsymbol{p}_a(0) = [1\ 0]^{\intercal}/[5L(0)]$, resulting in an out-of-plane tip deflection of -0.02 m in boom (a). The rest of the state and rate ICs are set to zero. A larger deployment rate than in the previous subsection is used, with the deployment profile $L(t) = 20 + 0.5t$ m. To avoid the numerical issues associated with the relatively small sail and its high deployment rate, large damping is used with $D = 10$.

Presented in Fig. 6 are snapshots of the major principal stress patterns for the simulation case in 2 s intervals from $t_0 = 0$ to $t_f = 10$ s. The predicted wrinkling patterns at each time are also provided in Fig. 7. Initially, the stresses increase toward the tip and create a completely taut sail quadrant, owing to the initial deflection of boom (a) only. However, as the boom tip bounds upward and the quadrant extends outward, irregularities in the distribution occur

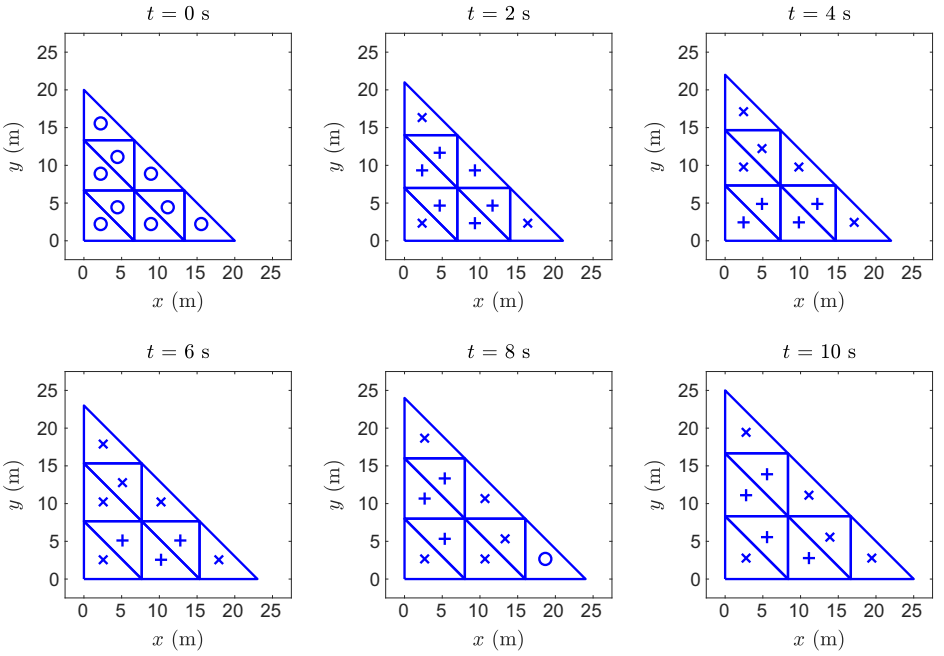

Fig. 7 Wrinkling states: circle (○) for taut, cross (×) for wrinkled, and plus (+) for slack, in the deploying quadrant of Subsection C.

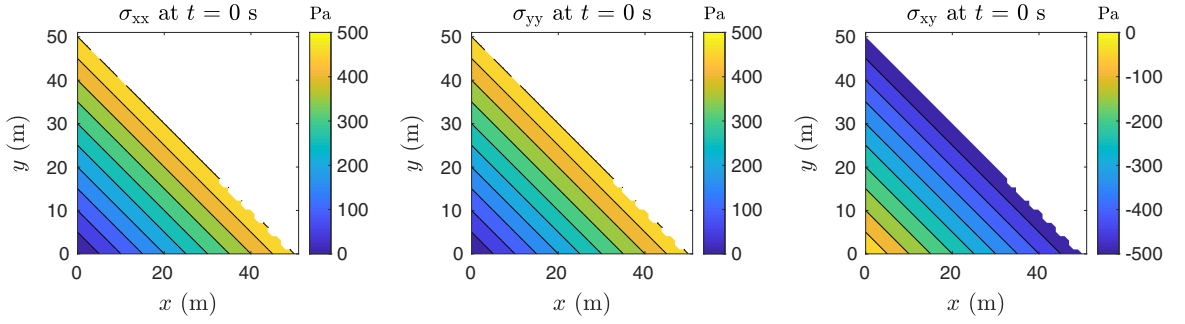

a) Linear model

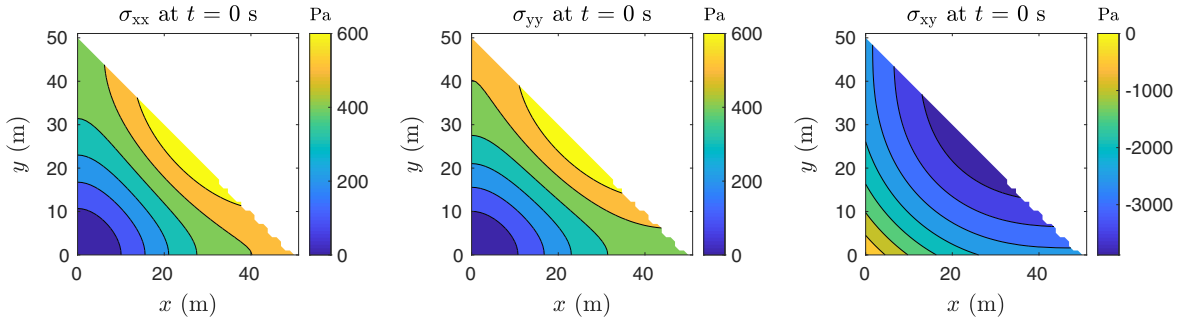

b) Nonlinear model with no wrinkling

Fig. 8 Initial stress components in the deploying quadrant of Subsection D with symmetric ICs, using both models.

throughout the sail, with the vicinity of the boom (a) tip continuing to have generally larger stresses. The reader should be cautioned not to interpret $t = 10$ s as the end of an actual deployment process, at which point one would expect mostly taut regions, because the system still has a nonzero extension rate of $\dot{L} = 0.5$ m/s. The presented results represent a snapshot of the motion, and not a complete deployment process. Treating full deployment would require allowing for nonzero accelerations, as well as much longer and computationally heavier simulations.

D. Comparison of Linear and Nonlinear Models

This section compares the results obtained using the nonlinear model of this study against those provided by the linear model of Vatankhahghadim and Damaren [16] to confirm they provide comparable results, and to assess the significance of the discrepancies between outputs of the two models. Several measures are used to make such a comparison meaningful: the wrinkling provisions in the nonlinear model are omitted, assuming the taut constitutive relation, $\boldsymbol{C}_T$ in Eq. (8), throughout the membrane and eliminating the need for a mesh; symmetric ICs are used, selected in a manner that the initial stress distribution at $t = 0$ of the nonlinear model matches the linearly increasing edge stresses assumed in [16] by the linear model; and a large Poisson's ratio of $\nu = 0.9$ is assumed by the nonlinear model, to increase the coupling between the in- and out-of-plane deflections and help with matching the initial stress distributions of the two models. This value is not realistic for a membrane, but the reader is reminded that the nonlinear model would have no problem with a smaller and more realistic ν, as demonstrated in the deploying quadrant results of Figs. 6 and 7, and the loaded membrane results of Fig. 14 presented later, all of which use $\nu \approx 0.3$. This choice is only made to allow for a meaningful comparison with the linear model that makes much more restrictive assumptions.

Other than $\nu = 0.9$, the rest of the parameters are set according to Table 1. The extension profile is set to $L(t) = 50 + 0.1t$ m, and a uniform membrane density of $\mu(x, y) = \mu_{\text{uni}} = 1.39 \times 10^{-2}$ kg/m^2 is assumed for simplicity and without affecting the intended comparison (especially given the nearly fully deployed nature of the test cases). Both models use $n_B = 3$ and $n_M = 9$ quasi modes for their

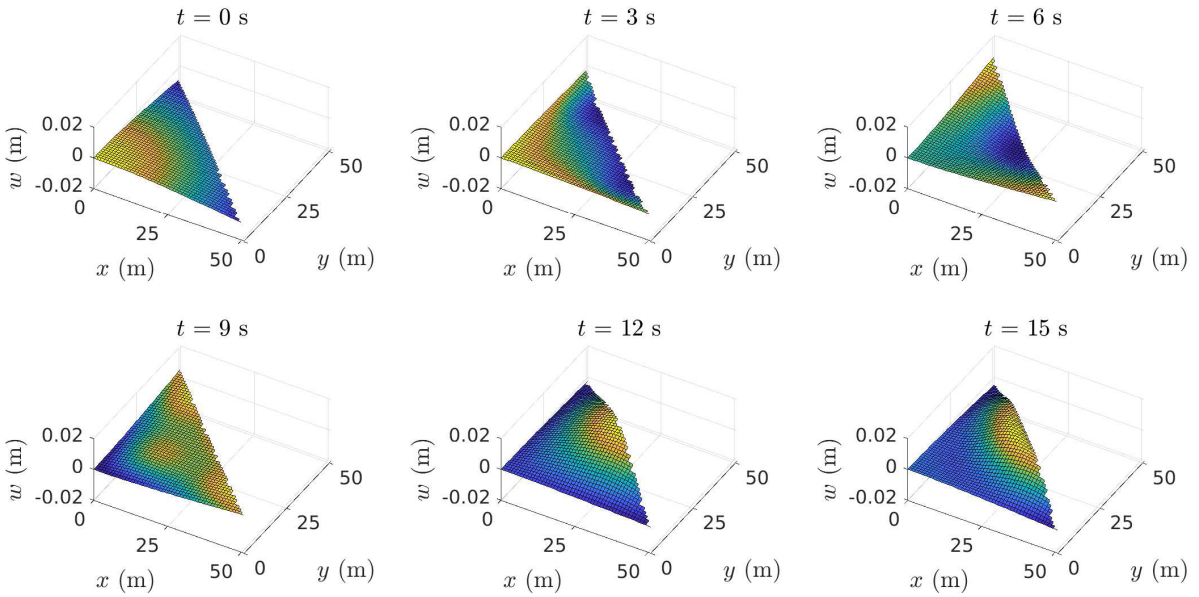

a) Linear model

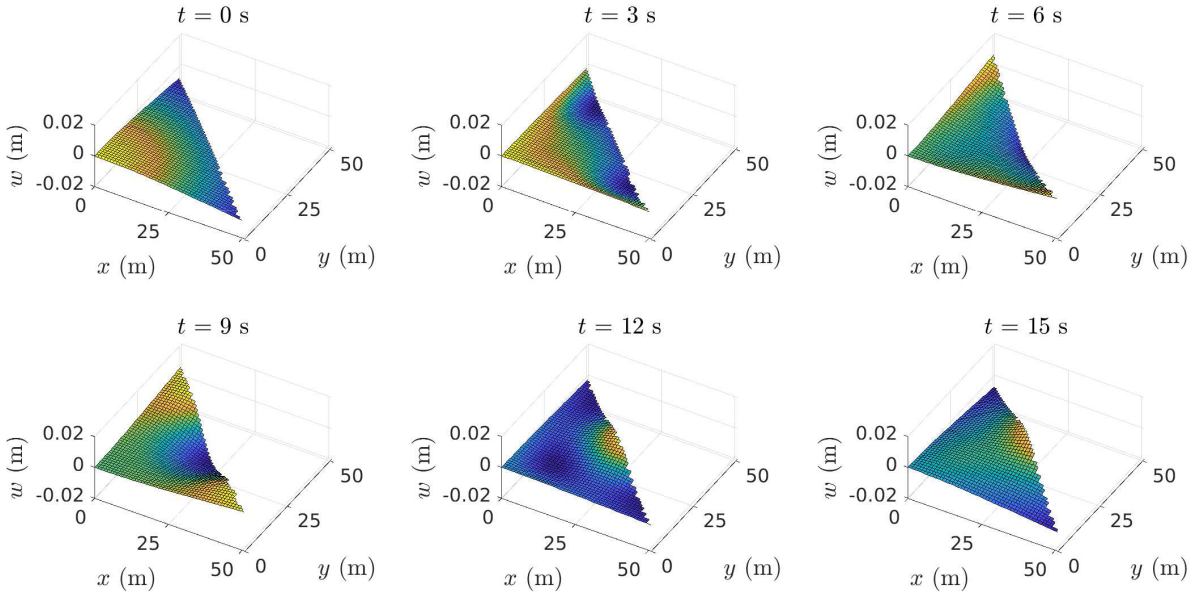

b) Nonlinear model with no wrinkling

Fig. 9 Out-of-plane membrane deflections in the deploying quadrant of Subsection D, using both models.

booms and membrane. The ICs of the booms are symmetrically set to $\boldsymbol{p}_a(0) = \boldsymbol{p}_b(0) = [1\ 0\ 0]^\intercal/[5L(0)]$ and $\boldsymbol{e}_a(0) = \boldsymbol{e}_b(0) = [1\ 0\ 0]^\intercal/[5L(0)] \times 10^{-2}$ with all the other ICs set to zero, resulting in small out-of- and in-plane boom tip deflections of -8 and -0.08 mm, respectively. To match the resulting stresses at $t = 0$, the assumed tip stress for the linear model is set to $\bar{\sigma} = 500$ Pa. No damping is used.

Shown in Fig. 8 are all three initial stress components for both models. Those in Fig. 8a are set by the selected $\bar{\sigma}$ and the analytical distribution obtained in [16], whereas those in Fig. 8b are the taut stress components calculated using the strains, in turn dictated by the judicious choice of ICs. Other than the curved regions around the free edge, they match quite well, but only at time $t = 0$. Whereas the stress components of the linear model maintain the same patterns as those in Fig. 8a, only increasing in magnitude during extension, the distributions obtained by the nonlinear model change quite significantly during the deployment, as shown later in Fig. 12. This highlights one of the advantages of the nonlinear model: the ability to more accurately predict the stress distribution.

The out-of-plane deflections throughout the membrane, obtained using both models, are shown in Fig. 9 and the online animations available as Supplementary Videos 1 and 2, corresponding to Figs. 9a and 9b, respectively. In addition, the out-of-plane tip deflections at the boom tips and the midpoint of the free edge of the membrane are plotted over time in Fig. 10. Comparing the membrane shapes predicted by both models, they show close match until about $t = 6$ s, after which they start to show obvious differences. However, the deflection profiles in Fig. 10 are promising: very close match is evident in Fig. 10a for the boom tips throughout the 15 s deployment, and although the values of the deflections in Fig. 10b at the representative point on the membrane do differ after $t = 6$ s, both models capture its increasing–decreasing pattern. Also noteworthy as a sanity check is the symmetry maintained by both models in response to the symmetric ICs. The same observation holds for the identical in-plane deflection patterns of the nonlinear model along both x and y directions, shown in Fig. 11. Also notable are the relative sizes of the out-of-plane and in-plane deflections, with the latter being two to three orders of magnitude smaller, as expected and as also reported in [33] for a moving membrane problem.

E. Validation Using Corner-Loaded Membrane Under Gravity

As another partial validation, the simulation results are compared against the experimental and numerical ones in [47,54], using a constant-size corner-loaded square membrane with no booms, illustrated in Fig. 13. To this end, the simplified EOM in Eq. (33) are modified to exclude the boom terms, drop the deployment terms, include the contributions from the external forces, and exploit the symmetry with equal loads on opposite corners. The reader is referred to [53] for the details of these modifications.

The physical parameters of the membrane are set to match those in [47,54]: $\mu = 3.75 \times 10^{-2}$ kg/m^2, $E = 3.5 \times 10^9$ N/m^2, $s = 2.5 \times 10^{-5}$ m, and $\nu = 0.31$. Considering the interest in the steady-state response only, large mass-proportional damping is used with $D = 10$. The numbers of modes and mesh elements per half-diagonal are $n_M = 4$ and $K = 4$ (resulting in 16 elements per quadrant), and the membrane ICs are all set to zero: $\boldsymbol{q}_{ab}(0) = \boldsymbol{f}_{ab}(0) = \boldsymbol{g}_{ab}(0) = \boldsymbol{0}_{4\times1}$ with zero rates. To avoid the numerical issues associated with the small membrane size of side length 0.5 m used in [47,54], a rescaled model with a side length of 10 m is used instead. As a consequence of this rescaling, the corner loads are set to vary between 100 and 400 N, namely, 20 times larger than the 5–20 N loads used in [47,54]. For numerical stability, the loads are applied gradually, using the profile in [43]: the corner loads are increased from 0 to 1% of the smaller intended load until $t = 0.2$ s, followed by the gravitational load applied from 0 to μg (per unit area, where g is the acceleration due to gravity) between $t = 0.2$ s to $t = 0.7$ s, followed by the remainder of the corner loads applied between $t = 0.7$ s to $t = 1.2$ s. The simulations then continue up to at least $t = 1.3$ s to allow the results to settle.

Shown in Fig. 14 are the predicted major principal stresses at the end of each load application scenario (at $t = 1.3$ s) for four different simulation cases: increasing T_2 on corners 2 and 4 (upper left and lower right) from 100 to 400 N, whereas T_1 remains the same value of 100 N on corners 1 and 3 in all cases. Comparing the stress

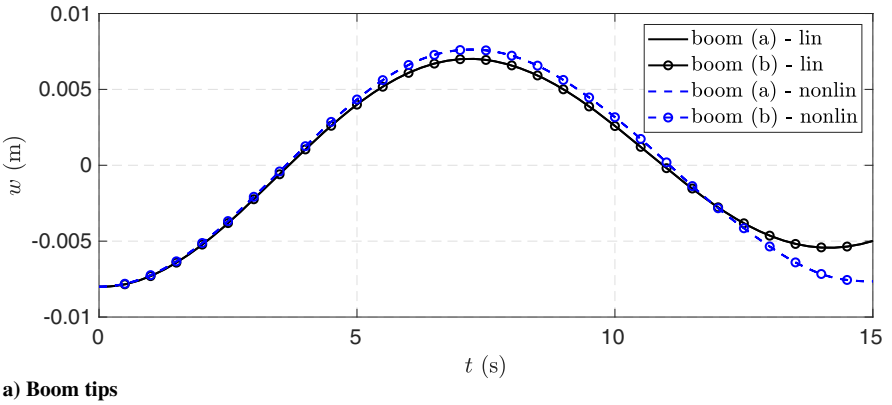

a) Boom tips

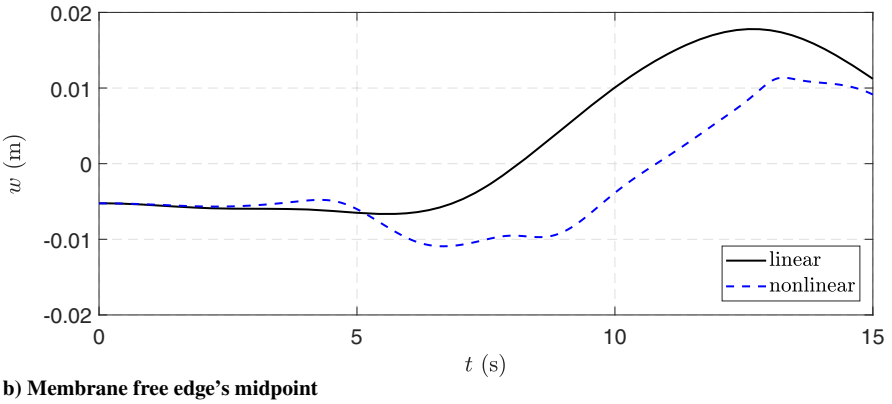

b) Membrane free edge's midpoint

Fig. 10 Out-of-plane deflections in the deploying quadrant of Subsection D, using both models.

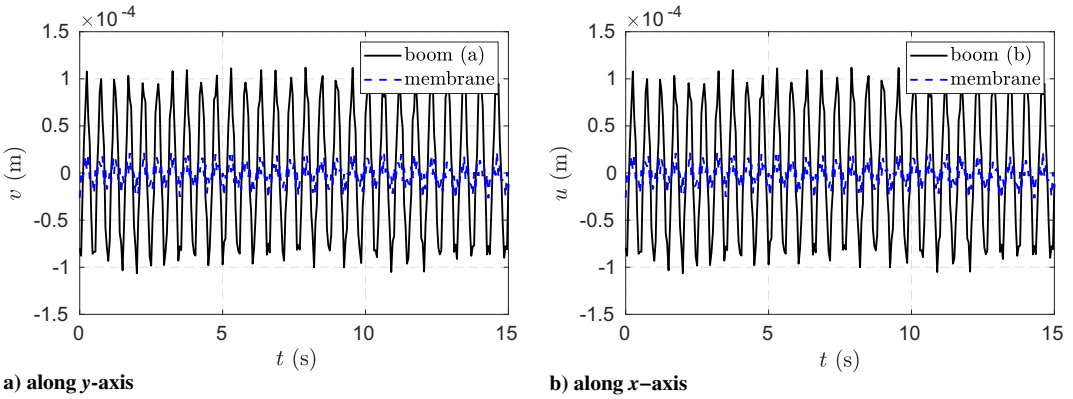

a) along y-axis b) along $x-$axis

Fig. 11 In-plane deflections at boom tips and midpoint of membrane edge in the deploying quadrant of Subsection D, using the nonlinear model with no wrinkling.

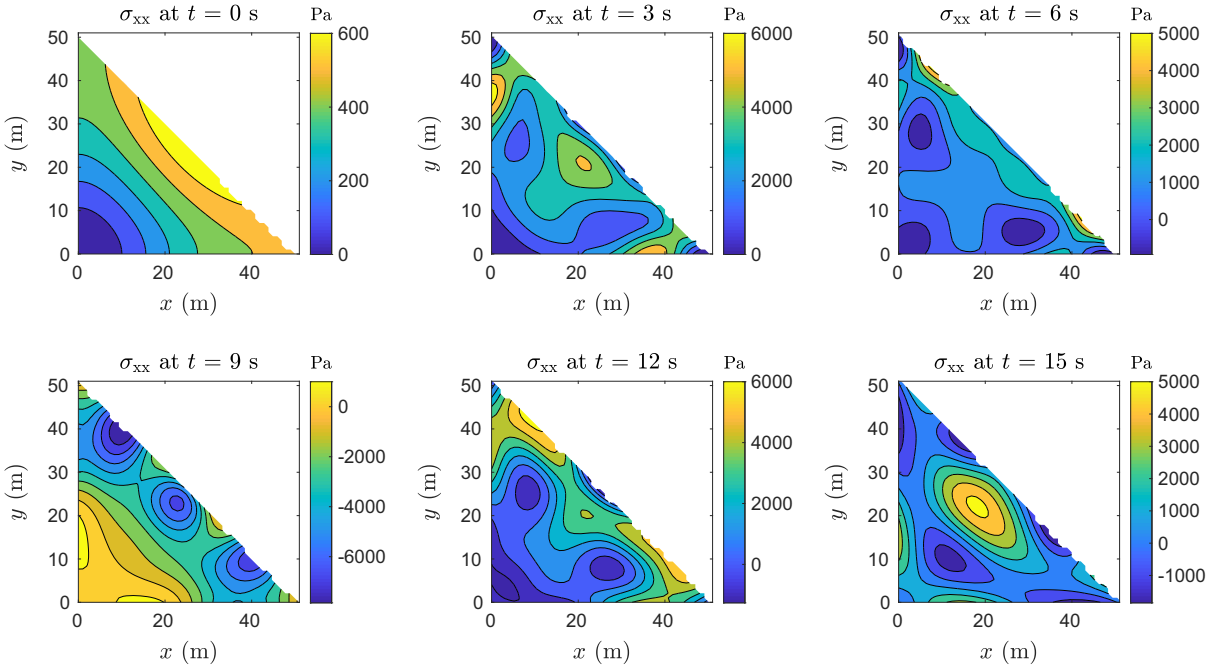

Fig. 12 Normal stress σ_{xx} in the deploying quadrant of Subsection D, using the nonlinear model with no wrinkling.

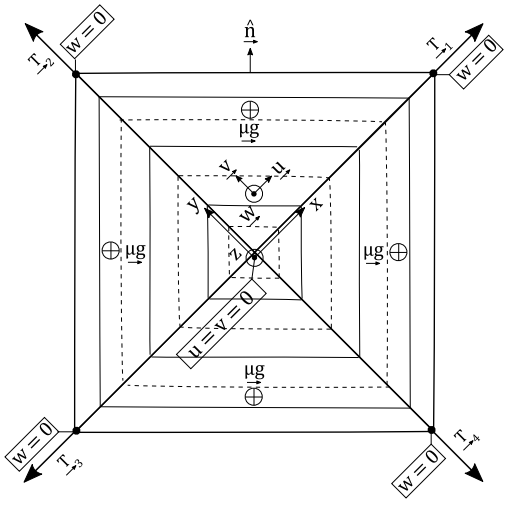

Fig. 13 Corner-loaded square membrane under gravity.

distributions in Fig. 14 to those in Fig. 19 of [47] (in turn validated with the experimental results in [54]), many similarities in their exhibited patterns are observed. For example, the high-stress corner regions, the low-stress regions near the middle of the side edges, the stress values of the same order of magnitude, as well as an increase in the stresses and their gradient as T_2 increases are all features shared by both figures. The predicted wrinkling states corresponding to the same simulation cases, as well as the cross-sectional profiles for out-of-plane deflections, the shapes of which are not captured well by the proposed model even though their orders of magnitude seem reasonable, can be found in [53].

VI. Conclusions

This paper treats the dynamics of a deploying (at a constant rate) quadrant of a boom-supported solar sail in a more complete manner than the previously published works, by also accounting for the in-plane deflections in addition to the out-of-plane ones, using nonlinear plate strains that couple the two deflection types and obtaining EOM that are nonlinear in states. The overall methodology is based on the quasi-modal expansion of the deflections: using both time- and

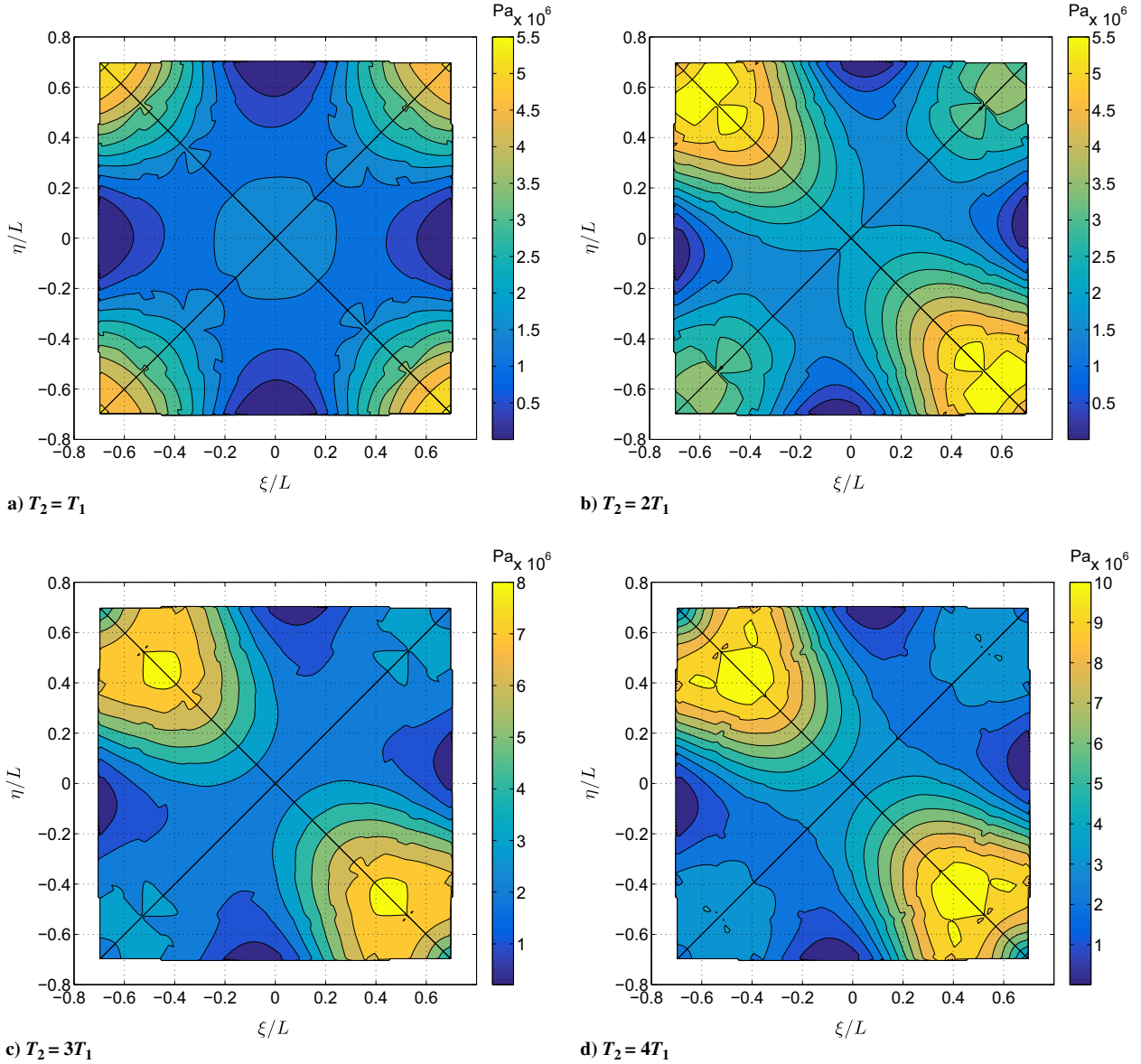

Fig. 14 Major principal stresses in the 10 m × 10 m membrane of Subsection E, under gravity and corner loads along its diagonals.

space-dependent basis functions that change with the size of the quadrant. Coordinate transformations and some algebraic operations are performed to make the required spatial integrals time invariant, thereby reducing the computational effort. In addition, an approach for making approximate wrinkling predictions using the Miller–Hedgepeth model and a coarse mesh (for wrinkling studies only) is also adopted in this paper. The presented simulation results assess the convergence of the wrinkling model in response to mesh refinement, and provide predictions of stress and wrinkling states in a sample deployment scenario. A constant-size loaded membrane that undergoes wrinkling is also considered, and the simulation results corresponding to it are compared against experimentally validated ones in literature. The predicted stresses match well.

A comparison of the results obtained using an earlier linear model, with only out-of-plane deflections, against those of the nonlinear model of this study is also performed. The conclusion from this comparison is that the linear model can help capture some of the essential features of the deployment dynamics, but only in special cases, in which its restrictive assumptions are reasonable. For example, to reproduce the stress distributions assumed by the linear model, symmetric ICs and a nonrealistically large Poisson's ratio were needed by the nonlinear model. It should be emphasized, however, that there is a relatively close match between the results even though there are significant discrepancies in the stress distributions of the two models after the initial time, as shown in Fig. 12. Achieving relatively close predictions using two models of varying complexity and sets of assumptions is promising and adds credibility to both models, but the discrepancy between some results suggests that the nonlinear model would be more suitable, if not required, for some applications, especially if the stress distributions are more important than the deflections.

Despite more or less similar results between the linear and nonlinear models, the nonlinear effects are not too small, and neglecting them can cause inaccuracies in the predictions. The appeal of the linear model is in its simplicity of implementation and very low computational cost: whereas the time integration portion of the reported comparison simulation took close to 7 h for the nonlinear model, the linear model handled the same test case in a few minutes on the same computer. This is because of the much larger number of generalized coordinates in the nonlinear model, as well as its need for calculating the nonlinear terms via large matrix multiplications. Therefore, depending on whether computational speed or accuracy is prioritized, each model has something extra to offer and both seem to have merit. However, the additional capabilities of the nonlinear model should not be overlooked: its assumptions are more permissive, and it can estimate the in-plane deflections and the wrinkling regions, neither of which is possible to predict using the linear model.

Acknowledgment

This research was supported by the Natural Sciences and Engineering Research Council of Canada through its Alexander Graham Bell Canada Graduate Scholarship–Doctoral program.

References

[1] Mote, C. D., Jr., "Dynamic Stability of Axially Moving Materials," *Shock and Vibration Digest*, Vol. 4, No. 4, 1972, pp. 2–11. https://doi.org/10.1177/058310247200400402

[2] Wickert, J. A., and Mote, C. D., Jr., "Current Research on the Vibration and Stability of Axially-Moving Materials," *Shock and Vibration Digest*, Vol. 20, No. 5, 1988, pp. 3–13. https://doi.org/10.1177/058310248802000503

[3] Zhu, W. D., "Vibration and Stability of Time-Dependent Translating Media," *Shock and Vibration Digest*, Vol. 32, No. 5, 2000, pp. 369–379. https://doi.org/10.1177/058310240003200502

[4] Wang, P. K. C., and Wei, J.-D., "Vibrations in a Moving Flexible Robot Arm," *Journal of Sound and Vibration*, Vol. 116, No. 1, 1987, pp. 149–160. https://doi.org/10.1016/S0022-460X(87)81326-3

[5] Bergamaschi, S., and Sinopoli, A., "On the Flexural Vibrations of Arms with Variable Length. An Exact Solution," *Mechanics Research Communications*, Vol. 10, No. 6, 1983, pp. 341–344. https://doi.org/10.1016/0093-6413(83)90062-9

[6] Stylianou, M., and Tabarrok, B., "Finite Element Analysis of an Axially Moving Beam, Part I: Time Integration," *Journal of Sound and Vibration*, Vol. 178, No. 4, 1994, pp. 433–453. https://doi.org/10.1006/jsvi.1994.1497

[7] Tabarrok, B., Leech, C. M., and Kim, Y. I., "On the Dynamics of an Axially Moving Beam," *Journal of the Franklin Institute*, Vol. 297, No. 3, 1974, pp. 201–220. https://doi.org/10.1016/0016-0032(74)90104-5

[8] Niemi, J., and Pramila, A., "FEM-Analysis of Transverse Vibrations of an Axially Moving Membrane Immersed in Ideal Fluid," *International Journal for Numerical Methods in Engineering*, Vol. 24, No. 12, 1987, pp. 2301–2313. https://doi.org/10.1002/nme.1620241205

[9] Koivurova, H., and Pramila, A., "Nonlinear Vibration of Axially Moving Membrane by Finite Element Method," *Computational Mechanics*, Vol. 20, No. 6, 1997, pp. 573–581. https://doi.org/10.1007/s004660050277

[10] Shin, C., Chung, J., and Kim, W., "Dynamic Characteristics of the Out-of-Plane Vibration for an Axially Moving Membrane," *Journal of Sound and Vibration*, Vol. 286, Nos. 4–5, 2005, pp. 1019–1031. https://doi.org/10.1016/j.jsv.2005.01.013

[11] Cherchas, D. B., "Dynamics of Spin-Stabilized Satellites During Extension of Long Flexible Booms," *Journal of Spacecraft and Rockets*, Vol. 8, No. 7, 1971, pp. 802–804. https://doi.org/10.2514/3.30323

[12] Cherchas, D. B., and Gossain, D. M., "Dynamics of a Flexible Solar Array During Deployment from a Spinning Spacecraft," *C.A.S.I. Transactions*, Vol. 7, No. 1, 1974, pp. 10–18.

[13] Hughes, P. C., "Deployment Dynamics of the Communications Technology Satellite—A Progress Report," *Proceedings of the ESRO Symposium on Dynamics and Control of Non-Rigid Spacecraft*, Vol. SP 117, European Space Agency, Neuilly, France, May 1976, pp. 335–340.

[14] Janković, M. S., "Deployment Dynamics of Flexible Spacecraft," Ph.D. Thesis, Univ. of Toronto, Toronto, 1979.

[15] Weeks, G. E., "Dynamic Analysis of a Deployable Space Structure," *Journal of Spacecraft and Rockets*, Vol. 23, No. 1, 1986, pp. 102–107. https://doi.org/10.2514/3.25090

[16] Vatankhahghadim, B., and Damaren, C. J., "Deployment of a Membrane Attached to Two Axially Moving Beams," *Journal of Applied Mechanics*, Vol. 86, No. 3, 2019, Paper 031003. https://doi.org/10.1115/1.4042134

[17] Tsuda, Y., Mori, O., Funase, R., Sawada, H., Yamamoto, T., Saiki, T., Endo, T., and Kawaguchi, J., "Flight Status of IKAROS Deep Space Solar Sail Demonstrator," *Acta Astronautica*, Vol. 69, Nos. 9–10, 2011, pp. 833–840. https://doi.org/10.1016/j.actaastro.2011.06.005

[18] Spencer, D. A., Betts, B., Bellardo, J. M., Diaz, A., Plante, B., and Mansell, J. R., "The LightSail 2 Solar Sailing Technology Demonstration," *Advances in Space Research*, Vol. 67, No. 9, 2021, pp. 2878–2889. https://doi.org/10.1016/j.asr.2020.06.029

[19] Mansell, J. R., Spencer, D. A., Plante, B. A., Fernandez, M. A., Gillespie, C. T., Bellardo, J. M., Diaz, A., Betts, B., and Nye, B., "Orbit and Attitude Performance of the LightSail 2 Solar Sail Spacecraft," *AIAA Guidance, Navigation, and Control Conference, SciTech Forum*, AIAA Paper 2020-2177, Jan. 2020. https://doi.org/10.2514/6.2020-2177.

[20] Wilkie, W. K., Fernandez, J. M., Stohlman, O. R., Schneider, N. R., Dean, G. D., Kang, J. H., Warren, J. E., Cook, S. M., Brown, P. L., Denkins, T. C., Horner, S. D., Tapio, E. D., Straubel, M., Richter, M., and Heiligers, J., "An Overview of the NASA Advanced Composite Solar Sail (ACS3) Technology Demonstration Project," *AIAA SciTech Forum*, AIAA Paper 2021-1260, Jan. 2021. https://doi.org/10.2514/6.2021-1260

[21] Vatankhahghadim, B., and Damaren, C. J., "Solar Sail Deployment Dynamics," *Advances in Space Research*, Vol. 67, No. 9, 2021, pp. 2746–2756. https://doi.org/10.1016/j.asr.2020.03.029

[22] Hassanpour, S., and Damaren, C. J., "Linear Structural Dynamics and Modal Cost Analysis for a Solar Sail," *AIAA Spacecraft Structures Conference, SciTech Forum*, AIAA Paper 2018-1434, Jan. 2018. https://doi.org/10.2514/6.2018-1434

[23] Jenkins, C. H., and Leonard, J. W., "Nonlinear Dynamic Response of Membranes: State of the Art," *Applied Mechanics Reviews*, Vol. 44, No. 7, 1991, pp. 319–328. https://doi.org/10.1115/1.3119506

[24] Jenkins, C. H., "Nonlinear Dynamic Response of Membranes: State of the Art—Update," *Applied Mechanics Reviews*, Vol. 49, No. 10S, 1996, pp. S41–S48. https://doi.org/10.1115/1.3101975

[25] Wickert, J. A., "Non-Linear Vibration of a Traveling Tensioned Beam," *International Journal of Non-Linear Mechanics*, Vol. 27, No. 3, 1992, pp. 503–517. https://doi.org/10.1016/0020-7462(92)90016-Z

[26] Zhang, L., and Zu, J. W., "Nonlinear Vibration of Parametrically Excited Moving Belts, Part I: Dynamic Response," *Journal of Applied Mechanics*, Vol. 66, No. 2, 1999, pp. 396–402. https://doi.org/10.1115/1.2791062

[27] Behdinan, K., Stylianou, M. C., and Tabarrok, B., "Dynamics of Flexible Sliding Beams—Non-Linear Analysis Part I: Formulation," *Journal of Sound and Vibration*, Vol. 208, No. 4, 1997, pp. 517–539. https://doi.org/10.1006/jsvi.1997.1167

[28] Ghayesh, M. H., Amabili, M., and Païdoussis, M. P., "Nonlinear Dynamics of Axially Moving Plates," *Journal of Sound and Vibration*, Vol. 332, No. 2, 2013, pp. 391–406. https://doi.org/10.1016/j.jsv.2012.08.013

[29] Farag, N. H., and Pan, J., "Modal Characteristics of In-Plane Vibration of Rectangular Plates," *Journal of the Acoustical Society of America*, Vol. 105, No. 6, 1999, pp. 3295–3310. https://doi.org/10.1121/1.424658

[30] Wang, G., and Wereley, N. M., "Free In-Plane Vibration of Rectangular Plates," *AIAA Journal*, Vol. 40, No. 5, 2002, pp. 953–959. https://doi.org/10.2514/2.1732

[31] Gorman, D. J., "Free In-Plane Vibration Analysis of Rectangular Plates by the Method of Superposition," *Journal of Sound and Vibration*, Vol. 272, Nos. 3–5, 2004, pp. 831–851. https://doi.org/10.1016/S0022-460X(03)00421-8

[32] Shin, C., Kim, W., and Chung, J., "Free In-Plane Vibration of an Axially Moving Membrane," *Journal of Sound and Vibration*, Vol. 272, Nos. 1–2, 2004, pp. 137–154. https://doi.org/10.1016/S0022-460X(03)00323-7

[33] Shin, C., Chung, J., and Yoo, H. H., "Dynamic Responses of the In-Plane and Out-of-Plane Vibrations for an Axially Moving Membrane," *Journal of Sound and Vibration*, Vol. 297, Nos. 3–5, 2006, pp. 794–809. https://doi.org/10.1016/j.jsv.2006.04.031

[34] McIver, D. B., "Hamilton's Principle for Systems of Changing Mass," *Journal of Engineering Mathematics*, Vol. 7, No. 3, 1973, pp. 249–261. https://doi.org/10.1007/BF01535286

[35] Miyazaki, Y., "Wrinkle/Slack Model and Finite Element Dynamics of Membrane," *International Journal for Numerical Methods in Engineering*, Vol. 66, No. 7, 2006, pp. 1179–1209. https://doi.org/10.1002/nme.1588

[36] Roddeman, D. G., Drukker, J., Oomens, C. W. J., and Janssen, J. D., "The Wrinkling of Thin Membranes: Part I—Theory," *Journal of Applied Mechanics*, Vol. 54, No. 4, 1987, pp. 884–887. https://doi.org/10.1115/1.3173133

[37] Epstein, M., and Forcinito, M. A., "Anisotropic Membrane Wrinkling: Theory and Analysis," *International Journal of Solids and Structures*, Vol. 38, Nos. 30–31, 2001, pp. 5253–5272. https://doi.org/10.1016/S0020-7683(00)00346-2

[38] Kang, S., and Im, S., "Finite Element Analysis of Dynamic Response of Wrinkling Membranes," *Computer Methods in Applied Mechanics and*

Engineering, Vol. 173, Nos. 1–2, 1999, pp. 227–240.
https://doi.org/10.1016/S0045-7825(98)00271-0

[39] Miller, R. K., and Hedgepeth, J. M., "An Algorithm for Finite Element Analysis of Partly Wrinkled Membranes," *AIAA Journal*, Vol. 20, No. 12, 1982, pp. 1761–1763.
https://doi.org/10.2514/3.8018

[40] Stein, M., and Hedgepeth, J. M., "Analysis of Partly Wrinkled Membranes," NASA TN D-813, July 1961.

[41] Miyazaki, Y., and Iwai, Y., "Dynamics Model of Solar Sail Membrane," *ISAS Proceedings of 14th Workshop on Astrodynamics and Flight Mechanics 2004: A Collection of Technical Papers*, Japan Aerospace Exploration Agency Inst. of Space and Astronautical Science, Sagamihara, Japan, 2005.

[42] Wang, C. G., and Du, X. W., "Wrinkle Analysis of Space Membrane Structures and Applications," *International Journal for Computational Methods in Engineering Science and Mechanics*, Vol. 8, No. 3, 2007, pp. 159–164.
https://doi.org/10.1080/15502280701252594

[43] Choi, M., "Flexible Dynamics and Attitude Control of a Square Solar Sail," Ph.D. Thesis, Univ. of Toronto, Toronto, 2015.

[44] Murphy, D. M., Murphey, T. W., and Gierow, P. A., "Scalable Solar-Sail Subsystem Design Concept," *Journal of Spacecraft and Rockets*, Vol. 40, No. 4, 2003, pp. 539–547.
https://doi.org/10.2514/2.3975

[45] Greschik, G., Derbes, B., Veal, G., and Rogan, J., "The Cord Mat Sail—Concept, Mechanics, and Design Example," *46th AIAA/ASME/ASCE/AHS/ASC Structures, Structural Dynamics and Materials Conference*, AIAA Paper 2005-2049, April 2005.
https://doi.org/10.2514/6.2005-2049

[46] Barnes, N. C., Derbes, W. C., Player, C. J., and Diedrich, B. L., "Sunjammer: A Solar Sail Demonstration," *Advances in Solar Sailing*, edited by M. Macdonald, Springer Praxis Books, Springer, Berlin, 2014, pp. 115–126.
https://doi.org/10.1007/978-3-642-34907-2

[47] Wong, W., and Pellegrino, S., "Wrinkled Membranes. Part III: Numerical Simulations," *Journal of Mechanics of Materials and Structures*, Vol. 1, No. 1, 2006, pp. 61–93.
https://doi.org/10.2140/jomms.2006.1.63

[48] Amabili, M., *Nonlinear Vibrations and Stability of Shells and Plates*, Cambridge Univ. Press, Cambridge, New York, 2008, Chap. 1.
https://doi.org/10.1017/CBO9780511619694

[49] Miller, R. K., Hedgepeth, J. M., Weingarten, V. I., Das, P., and Kahyai, S., "Finite Element Analysis of Partly Wrinkled Membranes," *Computers & Structures*, Vol. 20, Nos. 1–3, 1985, pp. 631–639.
https://doi.org/10.1016/0045-7949(85)90111-7

[50] Shaker, F. J., "Free-Vibration Characteristics of a Large Split-Blanket Solar Array in a 1-g Field," NASA TN D-8376, Dec. 1976.

[51] Hildebrand, F. B., *Methods of Applied Mathematics*, Prentice–Hall, New York, 1952, Sec. 1.28.

[52] Kane, T. R., Likins, P. W., and Levinson, D. A., *Spacecraft Dynamics*, McGraw–Hill, New York, 1983, Sec. 4.10.

[53] Vatankhahghadim, B., "Deployment Dynamics and Stability of a Boom-Supported Solar Sail," Ph.D. Thesis, Univ. of Toronto, Toronto, 2021.

[54] Wong, W., and Pellegrino, S., "Wrinkled Membranes. Part I: Experiments," *Journal of Mechanics of Materials and Structures*, Vol. 1, No. 1, 2006, pp. 3–25.
https://doi.org/10.2140/jomms.2006.1.3

V. Babuska
Associate Editor